A&A 579, A101 (2015)
DOI: 10.1051/0004-6361/201424918

Astronomy & Astrophysics

Lambda = 3 mm line survey of nearby active galaxies⋆,⋆⋆

R. Aladro[1], S. Martín[2], D. Riquelme[3], C. Henkel[3,4], R. Mauersberger[1], J. Martín-Pintado[5], A. Weiß[3], C. Lefevre[6], C. Kramer[7], M. A. Requena-Torres[3], and R. J. Armijos-Abendaño[5,8]

[1] European Southern Observatory, Avda. Alonso de Córdova 3107, Vitacura, Santiago, Chile
e-mail: raladro@eso.org
[2] Institut de Radio Astronomie Millimétrique, 300 rue de la Piscine, Dom. Univ., 38406 St.-Martin d'Hères, France
[3] Max-Planck-Institut für Radioastronomie, Auf dem Hügel 69, 53121 Bonn, Germany
[4] Astron. Dept., King Abdulaziz University, PO Box 80203, 21589 Jeddah, Saudi Arabia
[5] Centro de Astrobiología (CSIC-INTA), Ctra. de Torrejón Ajalvir km 4, 28850 Torrejón de Ardoz, Madrid, Spain
[6] LERMA2 & UMR 8112 du CNRS, Observatoire de Paris, 61 Av. de l'Observatoire, 75014 Paris, France
[7] Instituto de Radioastronomía Milimétrica, Avda. Divina Pastora 7, Local 20, 18012 Granada, Spain
[8] Observatorio Astronómico de Quito, Escuela Politécnica Nacional, Av. Gran Colombia S/N, Interior del Parque La Alameda, 170136 Quito, Ecuador

Received 4 September 2014 / Accepted 14 April 2015

ABSTRACT

Aims. We aim to better understand the imprints that the nuclear activity in galaxies leaves in the molecular gas.
Methods. We used the IRAM 30 m telescope to observe the frequency range ~[86−116] GHz towards the central regions of the starburst galaxies M 83, M 82, and NGC 253, the galaxies hosting an active galactic nucleus (AGN) M 51, NGC 1068, and NGC 7469, and the ultra-luminous infrared galaxies (ULIRGs) Arp 220 and Mrk 231. Assuming local thermodynamic equilibrium (LTE), we calculated the column densities of 27 molecules and 10 isotopologues (or their upper limits in case of non-detections).
Results. Among others, we report the first tentative detections of CH_3CHO, HNCO, and NS in M 82 and, for the first time in the extragalactic medium, HC_5N in NGC 253. Hα recombination lines were only found in M 82 and NGC 253. Vibrationally excited lines of HC_3N were only detected in Arp 220. CH_3CCH emission is only seen in the starburst-dominated galaxies. By comparison of the fractional abundances among the galaxies, we looked for the molecules that are best suited to characterise the chemistry of each group of galaxies (starbursts, AGNs and ULIRGs), as well as the differences among galaxies within the same group.
Conclusions. Suitable species for characterising and comparing starburst galaxies are CH_3OH and HNCO as tracers of large-scale shocks, which dominate early to intermediate starburst stages, and CH_3CCH, c-C_3H_2, and HCO as tracers of UV fields, which control the intermediate-to-old or post starburst phases. M 83 shows signs of a shock-dominated environment. NGC 253 is characterised by both strong shocks and some UV fields. M 82 stands out for its bright photo-dissociated region tracers, which indicate an UV field-dominated environment. Regarding AGNs, the abundances of HCN and CN (previously claimed as enhanced in AGNs) in M 51 are similar to those in starburst galaxies, while the HCN/HCO^+ ratio is high in M 51 and NGC 1068, but not in NGC 7469. We did not find a correlation between the HCN/CS ratio (recently claimed as a possible starburst/AGN discriminator) and the AGN activity. However, a high enough spatial resolution to separate their circumnuclear disks from the surrounding star-forming regions is needed to find molecular abundance trends in AGNs. High abundances of $H^{13}CN$ and HC_3N, as well as a similarity between the column densities of ^{13}CO and $C^{18}O$, are representative of the molecular interstellar medium in the ULIRGs. Furthermore, the chemistry of Arp 220 points towards a more starburst-dominated environment, while that of Mrk 231 more resembles the AGNs of our sample.

Key words. ISM: molecules – galaxies: ISM – galaxies: nuclei – galaxies: active – galaxies: abundances – radio lines: ISM

1. Introduction

The creation and destruction of molecular species in the dense interstellar medium (ISM) are directly related to a number of physical mechanisms, namely large-scale shocks, cosmic rays, UV radiation fields, and X-rays. Hence, studying molecular abundances can be a way to infer the importance of these processes for the star formation and to understand how they favour dispersion or gravitational collapse of compact clouds or their ionisation. In the particular case of the dense gas found to surround galactic nuclei, one can even attempt to deduce the nature of their powering sources using millimetre (mm) or sub-mm spectra (e.g. Martín et al. 2011).

From comparing chemical models with observations, it has been claimed that the abundances of some species, such as HCN and CN, are enhanced in the presence of X-rays and cosmic-ray ionisation fields that are dominant in active galactic nuclei (AGNs, Kohno et al. 2001; Meijerink et al. 2007; Krips et al. 2008; Aladro et al. 2013; Izumi et al. 2013). On the other hand, less energetic radiation from UV fields destroys heavy molecules such as HNCO and CH_3OH (Martín et al. 2006a, 2008, 2009a), while at the same time it helps creating others that are formed through ion-molecule reactions, such as c-C_3H_2, CO^+ or HOC^+ (e.g. Savage & Ziurys 2004; Martín et al. 2009a; Aladro et al. 2011b). Shocks caused by stellar winds, supernovae, or molecular cloud collapse can release species formed on dust grains to the gaseous phase (e.g. CH_3OH, HNCO, or sulfur-bearing

⋆ Appendix A is available in electronic form at http://www.aanda.org
⋆⋆ FITS files of the reduced spectra are only available at the CDS via anonymous ftp to cdsarc.u-strasbg.fr (130.79.128.5) or via http://cdsarc.u-strasbg.fr/viz-bin/qcat?J/A+A/579/A101

Table 1. Main properties of the galaxies.

Galaxy	α (J 2000) h:m:s	δ (J 2000) °:′:″	D^a Mpc	$V_{\rm LSR}{}^b$ km s^{-1}	$\theta_s{}^c$ ″ /pc	$SFR^{(d)}$ $M_\odot$ yr^{-1}	$L^e_{\rm IR}$ $L_\odot$	Activity type
M 83	13:37:00.93	–29:51:56.40	4.5	513	15/327	2.5	1.2×10^{10}	Starburst
NGC 253	00:47:33.12	–25:17:18.60	3.9	250	20/378	3.6	2.8×10^{10}	Starburst
M 82-NE	09:55:51.90	69:40:47.00	3.5	300	12 /204	10	5.9×10^{10}	Starburst
M 51	13:29:52.70	47:11:43.00	8.4	470	15/611	2.5	2.6×10^{10}	AGN
NGC 1068	02:42:40.90	–00:00:46.00	14.4	1100	4/279	0.4	1.9×10^{11}	AGN + Starburst
NGC 7469	23:03:15.60	08:52:26.00	29.5	4892	6/858	30	3.9×10^{11}	AGN + Starburst
Arp 220	15:34:57.08	23:30:11.30	70.0	5350	2/679	240	1.6×10^{12}	Starburst
Mrk 231	12:56:14.20	56:52:25.00	170.0	12 173	2/1640	220	3.2×10^{12}	AGN

Notes. For M 82 we observed the north-eastern (NE) molecular lobe at an offset position $(\Delta\alpha, \Delta\delta) = (+13.0'', +7.5'')$ with respect to its dynamical centre. $^{(a)}$ Distances taken from the NASA/IPAC Extragalactic Database; $^{(b)}$ systemic local standard of rest (LSR) radial velocities following the optical convention, taken from SIMBAD; $^{(c)}$ source sizes and their corresponding spatial scales for the assumed distances; $^{(d)}$ star formation rate obtained from Walter et al. (2008) for M 83; Strickland et al. (2004) for NGC 253 and M 82; Schuster et al. (2007) for M 51; Esquej et al. (2014) for NGC 1068; Genzel et al. (1995) for NGC 7469; Anantharamaiah et al. (2000) for Arp 220; Taylor et al. (1999) for Mrk 231. We note that this parameter is only meant to give a rough idea of the activity, as it was calculated for different volumes in each galaxy. ^{e} Infrared luminosities taken from Sanders et al. (2003).

species, Viti et al. 2001; Martín et al. 2009a; Jiménez-Serra et al. 2008).

Unbiased extragalactic molecular line surveys at mm wavelengths (Martín et al. 2006b; Muller et al. 2011; Aladro et al. 2011b, 2013; Davis et al. 2013; Watanabe et al. 2014) allow us to observe many species simultaneously and identify those that provide the best information about the physical properties around the nuclear regions of active galaxies. Some molecules much less abundant than the commonly observed species, CO, HCN or HCO^+, seem to be more sensitive to their environments and show larger differences in their abundances among galaxy types. They can even be used to identify the evolutionary stage of galaxies. For example, the HNCO abundance varies by nearly two orders of magnitude between young and old starbursts and thus appears to be an excellent diagnostic tool of their evolutionary state (Martín et al. 2009a). CH_3CCH, on the other hand, is one of the most abundant species in starburst galaxies (even more than HCN and HCO^+), but has never been detected in any AGN-dominated source (Aladro et al. 2011a, 2013). Yet, extragalactic line surveys carried out so far have focused exclusively on a single type of galaxy, either starbursts (Martín et al. 2006b; Aladro et al. 2011b), luminous and ultra-luminous infrared galaxies ((U)LIRGs; Costagliola et al. 2011; Martín et al. 2011; Davis et al. 2013), or AGNs (Aladro et al. 2013). A detailed and uniform comparison of different types of active galaxies is still lacking in this context. Here, we therefore compare the molecular ISM in a sample of galaxies that includes starbursts, AGNs, and ULIRGs.

We present the first systematic unbiased spectral line survey of a sample of galaxies selected with respect to their nuclear activity. It is organised as follows: in Sect. 2 we introduce our galaxy sample. Section 3 describes the observations and data reduction. Section 4 details the data analysis, including a discussion of the molecular source sizes of the galaxies (Sect. 4.1), the line identification and line profiles (Sect. 4.2), spectral model fits, and rotational temperatures (Sect. 4.3). In Sect. 5 we summarise the detections (Sect. 5.1) and present the column densities calculated under the local thermodynamic equilibrium (LTE) assumption (Sect. 5.2). We indicate the potential key species for further extragalactic studies in Sect. 6. In Sect. 7 we detail our findings for starburst galaxies (Sect. 7.1), AGNs (Sect. 7.2), and ULIRGs (Sect. 7.3). Finally, we summarise our main conclusions in Sect. 8.

2. Galaxy sample

We selected a sample of eight galaxies based on their luminosity and galactic nuclear activity, following these characteristics: (a) the galaxies are in the local Universe ($z < 0.05$, $D <$ 200 Mpc); (b) they show bright molecular emission ($T_{\rm MB}^{\rm CO(1-0)} >$ 50 mK) and cover a wide range of infrared luminosity ($L_{\rm IR} = [10^9 - 10^{12}]\, L_\odot$), thus including low-luminosity galaxies, LIRGs and ULIRGs; (c) the sample encompasses the two main types of galactic nuclear activity: AGNs and starbursts; (d) it includes starbursts and ULIRGs in different stages of evolution; (e) it includes AGNs of both Seyfert (Sy) 1 and Sy 2 types. The eight galaxies are well-known extragalactic objects studied across almost the whole electromagnetic spectrum, and in particular at mm or sub-mm wavelengths. Moreover, these galaxies are often considered as archetypes in the local Universe of the different nuclear activities or stages of evolution mentioned above. Some of their main properties are listed in Table 1.

Our sample includes the three starburst galaxies M 83, NGC 253, and M 82. The last two were targets of line surveys at $\lambda = 2$ and 1.3 mm conducted with the IRAM 30 m telescope by Martín et al. (2006b) and Aladro et al. (2011b). These two studies confirmed that the molecular ISM in the north-eastern molecular lobe of M 82 shows typical features of an evolved starburst, where the gas is heavily pervaded by strong UV fields, while the nuclear region of NGC 253 is more influenced by low-velocity shocks. NGC 253 hosts notable large-scale outflows (Turner & Ho 1985; Bolatto et al. 2013), which indicate that its starburst is not in its initial state, but not as evolved as the starburst of M 82. With the present $\lambda = 3$ mm observations, these two galaxies are the best studied at millimetre wavelengths so far. We also observed M 83 as an example of a young starburst (Martín et al. 2009a). It has a lower star formation rate ($2.5\, M_\odot$ yr^{-1}, Walter et al. 2008) than NGC 253 and M 82, and a star formation episode lasting (only) around 6 Myr (Houghton & Thatte 2008). Thus its chemical composition is expected to be somewhat different from those of NGC 253 and M 82. With these three starburst galaxies, we aim to characterise better the changes of the molecular gas composition as the starburst processes evolve.

As galaxies containing AGNs, we include NGC 7469 (Sy 1), NGC 1068 (Sy 2), and M 51 (Sy 2). The results of the NGC 1068 survey were already published in Aladro et al. (2013), and we refer to that paper for a discussion of its isotopic line ratios and

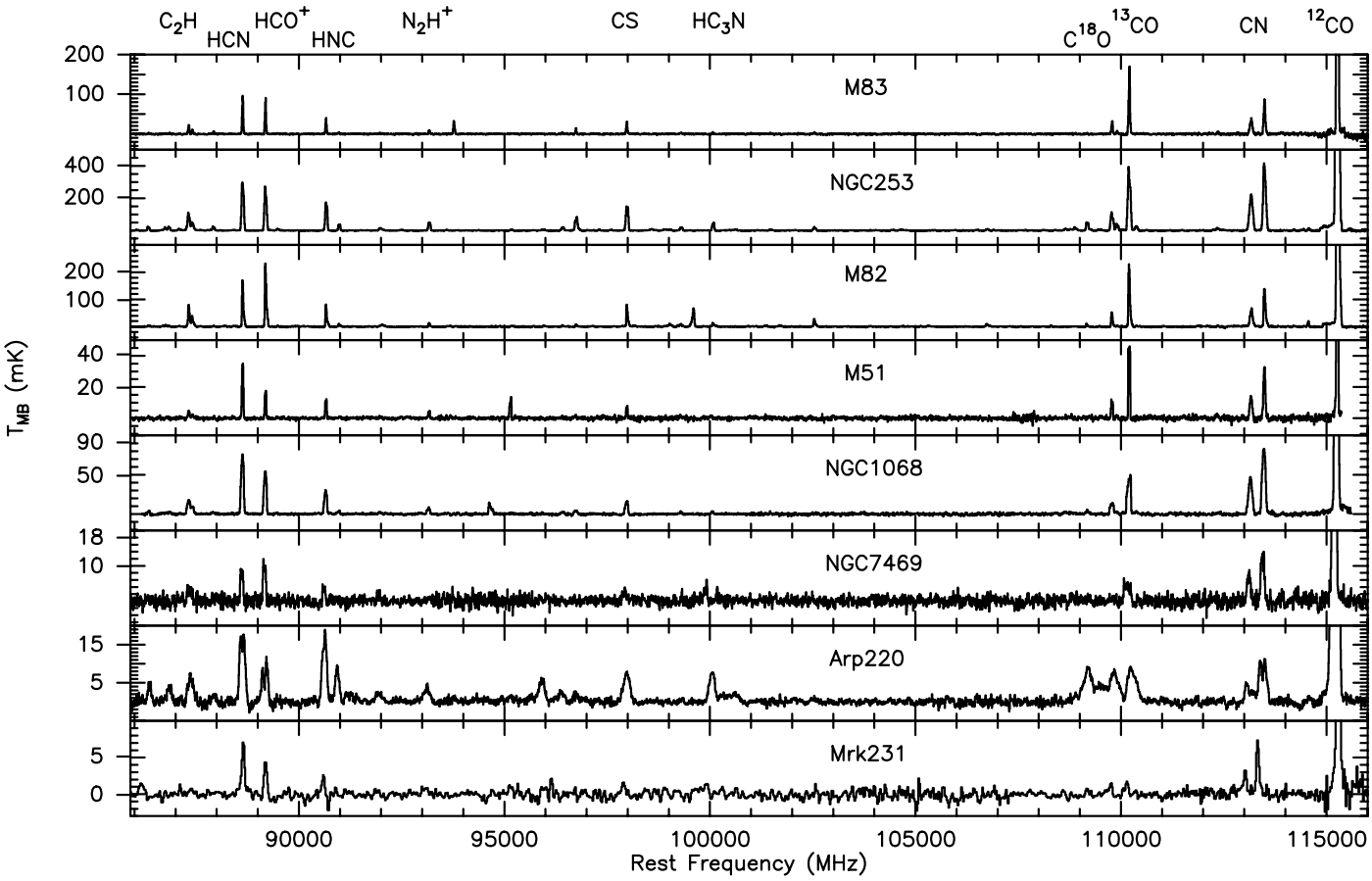

Fig. 1. Spectra of all eight galaxies between 86 and 116 GHz. The strongest molecules are indicated. The faint detected species are shown in Figs. 2 and 3. The spectra refer to the rest frame adopting the velocities in Table 1.

a chemical modelling of its central gas. Both NGC 7469 and NGC 1068 have a starburst ring at ∼1 kpc from the central AGN and very similar observed properties (see e.g. Table 2 of Wilson et al. 1991). On the other hand, M 51 shows several star-forming regions along its spiral arms (Bastian et al. 2005). In the three cases, the angular resolution of the 30 m beam (∼25″) did not allow us to separate the emission coming from the central AGNs and those of the surrounding starbursts. Thus, our data might be showing not only the molecular composition of their AGN, but also some contribution from the starburst regions. This might be particularly significant for NGC 7469 because of its farther distance, although estimations of the emission coming from starburst regions at our frequencies are only available for NGC 1068 (see details in Sect. 7.2).

To complement our sample, we observed two of the closest ULIRGs, Arp 220 and Mrk 231. Vigorous star-forming regions and black holes coexist in the centres of ULIRGs. Still, the main powering source of their nuclei remains unclear in most cases. Arp 220 is in an early stage of the merging process, with a double nucleus that is not resolved by our observations. An interferometric line survey made towards this galaxy by Martín et al. (2011) pointed to starburst processes as the more likely heating mechanism of its two centres (see also Greve et al. 2009). In contrast, Mrk 231 is in a later stage of merging, where the two nuclei of the individual galaxies are already fused, and molecular-rich large-scale outflows and super-winds are clearly present (Aalto et al. 2012). AGN activity probably prevails in this galaxy (e.g. Gallagher et al. 2002; van der Werf et al. 2010), and its nucleus seems to host a Sy 1 object (Boksenberg et al. 1977).

3. Observations and data reduction

The observations were carried out with the IRAM 30 m telescope[1] (Pico Veleta Observatory, Spain) between June 2009 and March 2012. We observed the eight galaxies in the frequency range ∼[86−116] GHz. For NGC 253 and M 82 we also included lower frequencies from 80 GHz and 85 GHz, respectively. The reduced spectra are shown in Figs. 1−5. The half-power beam width (HPBW) corresponding to the survey frequencies ranged from 29″ to 21″. We used the band E0 of the EMIR receiver (Carter et al. 2012) and the WILMA autocorrelator. This receiver-backend configuration allowed us to cover 8 GHz simultaneously in the two orthogonal linear polarisations and led to an original channel-width spacing of 5−7 km s^{-1}. The observed ∼30 GHz were covered by five tunings with a minimum overlap of 0.8 GHz. For some galaxies, an additional tuning was used to increase the signal-to-noise ratio in parts of the spectrum showing faint lines. The observations were made by wobbling the secondary mirror with a switching frequency of 0.5 Hz and a beam throw of 110″ in azimuth (80″ in the case of Arp 220).

The weather was variable during the different observing runs, from excellent (*pwv* ∼ 1 mm) to mediocre (*pwv* ∼ 6 mm) weather conditions. We checked the pointing accuracy every hour towards several nearby bright continuum sources. The pointing corrections were always <5″. The focus was also

[1] IRAM is supported by INSU/CNRS (France), MPG (Germany), and IGN (Spain).

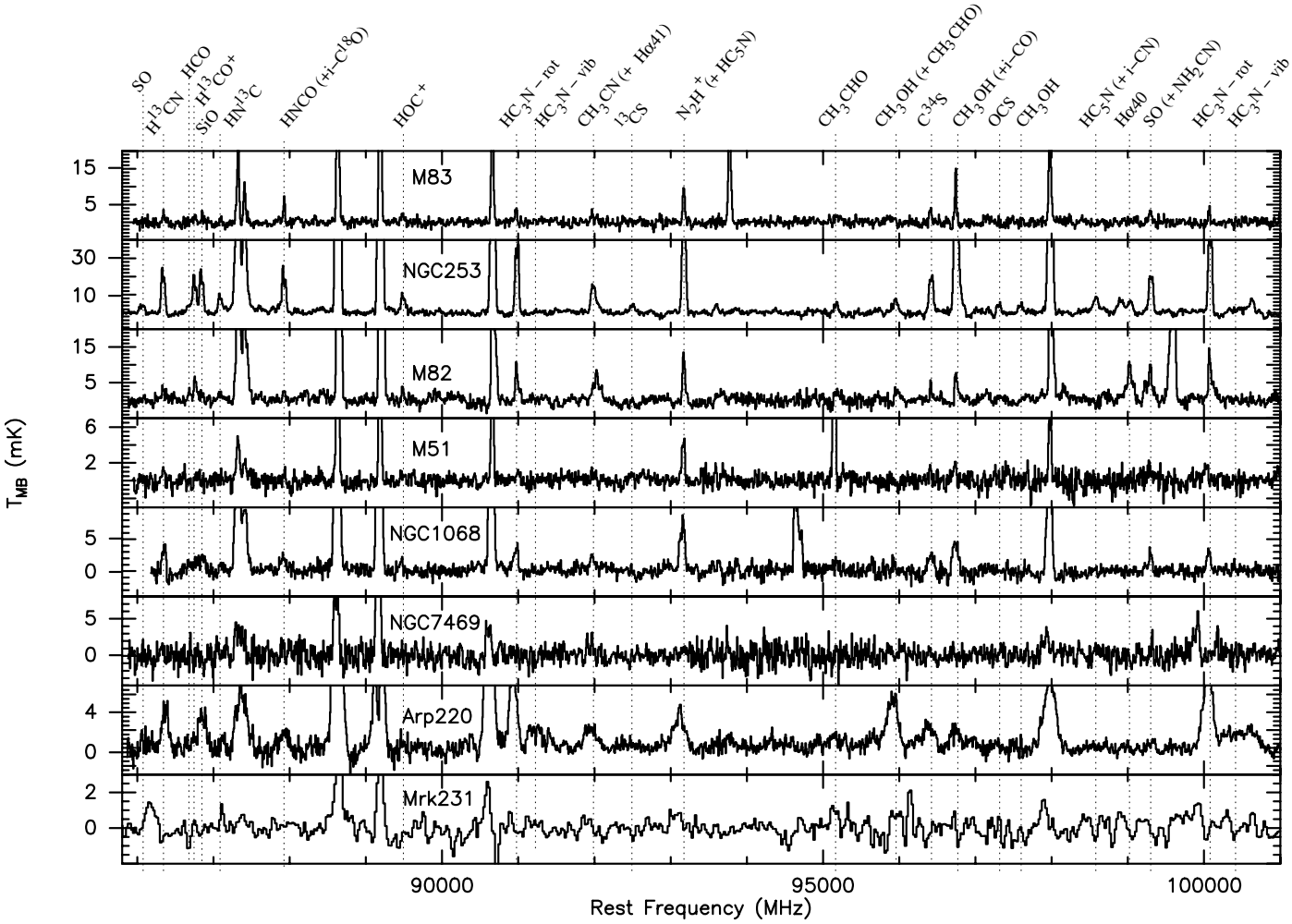

Fig. 2. Zoomed spectra between 86 GHz and 100 GHz where the faint detected lines are highlighted. Lines in brackets were not detected in all the galaxies (they were typically only detected in NGC 253). For details about the detections see Appendix A. The spectra refer to the rest frame adopting the velocities in Table 1.

checked and corrected at the beginning of each run and during sunsets and sunrises.

The data were first calibrated to the antenna temperature (T_A^*) scale using the chopper-wheel method (Penzias & Burrus 1973). The observed spectra were then converted into main-beam temperatures (T_{MB}) using the relation $T_{MB} = (F_{eff}/B_{eff})\,T_A^*$, where F_{eff} is the forward efficiency of the telescope, whose values were between 0.94 and 0.95, and B_{eff} is the main-beam efficiency, ranging from 0.77 to 0.81[2].

Each individual spectrum was analysed separately. After eliminating bad channels or spectra containing strong ripples, all the spectra tuned at the same frequency were averaged and baselines of orders between zero and two were subtracted from each chunk of 8 GHz. We note, however, that for M 82 the baseline correction was not good enough to remove some small ripples in the range ~[107−109] GHz. Higher order baselines did not improve the resulting spectra. Fortunately, comparing its spectra with the rest of the galaxies shows that no important lines are expected in that range.

As a result of the broad line-widths of these galaxies (≥100 km s^{-1}), the final spectra of M 51, M 82, M 83, NGC 1068 and NGC 253 were smoothed to 11 − 14 km s^{-1}, those of Arp 220 and NGC 7469 were smoothed to 22−27 km s^{-1}, and the Mrk 231 data to ~60 km s^{-1}. The rms achieved for all galaxies was on average 1−2 mK (≤10 mJy beam^{-1}) across the whole survey at the final velocity resolutions. The data were also corrected to first order for beam dilution effects as

$$T_B = \left[\left(\theta_s^2 + \theta_b^2\right)/\theta_s^2\right] T_{MB}, \quad (1)$$

where T_B is the source averaged brightness temperature, θ_s is the molecular source size (see Table 1 and Sect. 4.1 for details), and θ_b is the beam size. Gaussian distribution of the emission was assumed. We did not correct the data for the gain-elevation curve and for the gain losses that are due to a large wobbler throw because these corrections are only minor at 3 mm wavelength.

4. Data analysis

4.1. Source sizes

The source size of the molecular emission in each galaxy can be estimated in two ways. One is through high angular resolution interferometric maps of the region of all the species, and the other is by comparison of the observations carried out with two

[2] http://www.iram.es/IRAMES/mainWiki/Iram30mEfficiencies

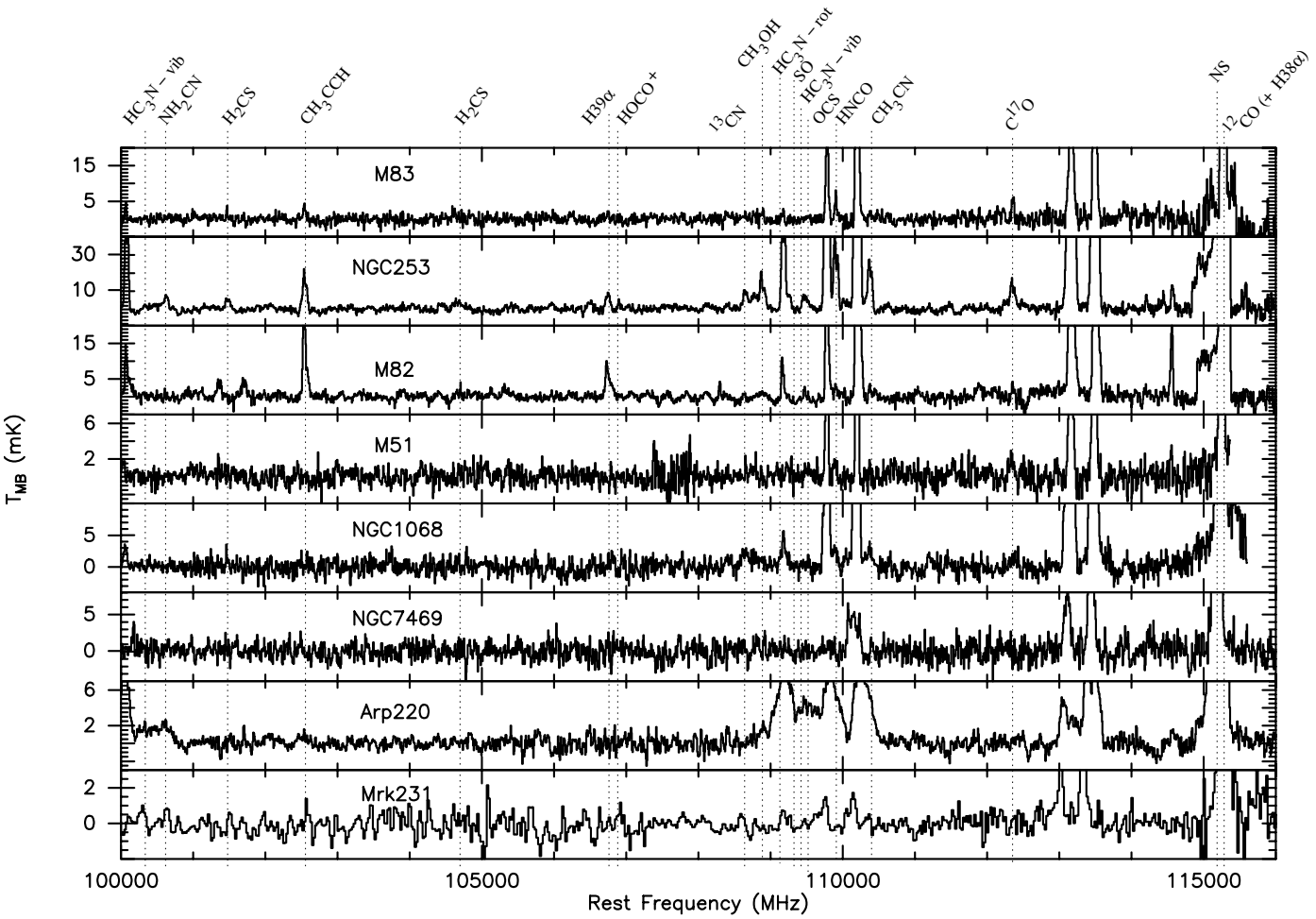

Fig. 3. Continued zoomed spectra between 100 GHz and 116 GHz where the faint detected lines are highlighted. Lines in brackets were not detected in all the galaxies (they were typically only detected in NGC 253). For details about the detections see Appendix A. The spectra refer to the rest frame adopting the velocities in Table 1.

(or more) telescopes having different beam sizes at the same frequency (so θ_s can be estimated from Eq. (1)). Unfortunately, the interferometric maps compiled so far for our sample of galaxies only encompass a few abundant species, such as CO, ^{13}CO, or HCN. In addition, most of the line transitions studied here were previously observed (if detected at all) with only one single-dish telescope.

To simplify the situation, we adopted the same source size for all the molecules detected in a galaxy. We estimated their θ_s from interferometric maps of ^{12}CO (1−0), HCN (1−0), HCO$^+$ (1−0), ^{13}CO (1−0), and HCO ($1_{01}-0_{00}$) (Downes & Solomon 1998, for Arp 220 and Mrk 231; Kohno et al. 1996, for M 51; García-Burillo et al. 2002, for the NE lobe of M 82; Muraoka et al. 2009, for M 83; Helfer & Blitz 1995; Schinnerer et al. 2000, for NGC 1068; Knudsen et al. 2007, for NGC 253; and Davies et al. 2004, for NGC 7469). The values are listed in Table 1.

The source size has a direct effect on the resulting brightness temperature (Eq. (1)), and consequently on the source-averaged column density. The larger (smaller) the source size that is assumed, the lower (higher) the column densities that are derived. To work around this, we base our discussion on column density ratios between species. Our estimates of these ratios would be only sensitive to differences in the emission extent between species, on which there is not enough information.

4.2. Line identification, line profiles, and Gaussian fits

We used the software MADCUBA_IJ[3] which includes the CDMS and JPL catalogues (Müller et al. 2001, 2005; Pickett et al. 1998), to identify the lines. The procedure was similar to what is described in detail in Aladro et al. (2011b) and also shown in the NGC 1068 survey (Aladro et al. 2013).

We used CLASS[4] to check whether there were lines coming from the image band of the spectra. The image band rejection of the E0 receiver is >10 dB, which ensures that most of the lines from the image band, except for the strongest ones, do not enter the signal band. We found that only the spectra from NGC 253, M 83 and M 82 are affected by features from the image band. A few of them were blended with other transitions from the signal band. Whenever the separation was large enough, we fixed the observed line parameters in the signal band to these to estimate their contribution to the image band line. Details of the fitting parameters are shown in Appendix A.

Of the eight galaxies, only M 83 and Mrk 231 show simple Gaussian line profiles. The bright lines in Arp 220 (e.g. HCN, HCO$^+$, CS) have a clear double-peak profile. It is not clear whether this might be due to the unresolved double nucleus or to absorption effects, as reported in previous interferometric

[3] http://cab.inta-csic.es/madcuba
[4] http://www.iram.fr/IRAMFR/GILDAS/

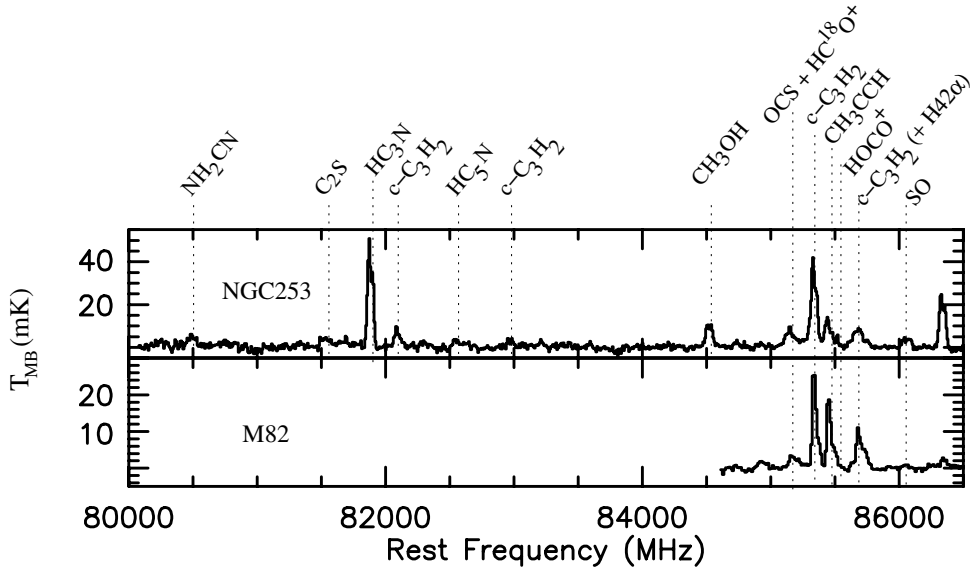

Fig. 4. Lowest frequency range observed exclusively towards NGC 253 and M 82 (the rest of the galaxies were observed from ~86 GHz).

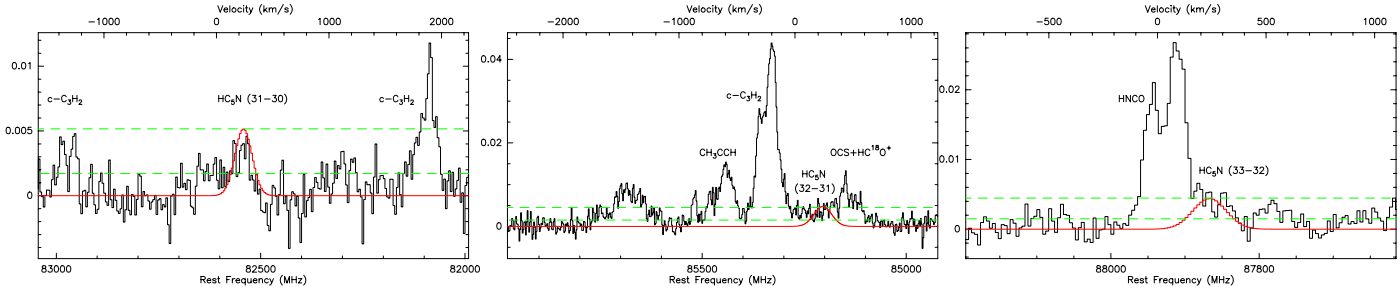

Fig. 5. Zoomed spectra of NGC 253 showing the Gaussian fits to the three strongest transitions of HC_5N detected tentatively. Dashed lines are 1σ and 3σ noise levels.

studies (Sakamoto et al. 2009; Tunnard et al. 2015). Fainter lines also show a deviation from Gaussian profiles, although not as clear as those that are optically thicker. Mrk 231 is also expected to be affected by absorption, but its lines are comparatively much fainter, and thus this effect, if present, is not as evident. The observed circumnuclear region of NGC 253 has five clumps of warm dense gas, but interferometric observations are needed to resolve them (e.g. Sakamoto et al. 2011). With the 30 m telescope, the integrated spectrum of NGC 253 appears as two blended Gaussians. On the other hand, the two-horned line profiles of M 51 and NGC 7469 include not only the emission from the very centre, but possibly also that coming from the inner arms and the surrounding molecular disks (Matsushita et al. 1998; Davies et al. 2004). NGC 1068 has a similar physical structure as NGC 7469 (a circumnuclear disk, surrounded by a starburst ring at ~1 kpc from the centre). In addition, the gas dynamics in the CND of NGC 1068 are quite complex, and some of the brightest lines, as seen by high-resolution observations, need several (two to four) Gaussian components to better fit the profiles (Krips et al. 2011; García-Burillo et al. 2014). Finally, while our M 82 observations are centred on the north-eastern (NE) molecular lobe of the nucleus, some emission from the very centre enters the 30 m beam. This translates into a bump at low velocities of some of the lines that we can easily separate from the NE emission (see Aladro et al. 2011b for details). To homogenize the data, we fitted a single Gaussian to all lines detected in the survey. This simplification has little effect on the derived column densities of the species, as shown by Martín et al. (2011) and Aladro et al. (2011a) for Arp 220 and NGC 253, respectively. However, we made sure that the results obtained by fitting one or more Gaussians to the lines give differences on the overall column densities that are lower than 10% of their values.

4.3. Spectral line model fit

Molecular emission was modelled using the SLIM package within MADCUBA_IJ (Martín et al., in prep.). The fit was performed in the parameter space of column density, rotational temperature, velocity, and width of the line to the actual emission. Thus integrated and peak line intensity, as well as opacity, are derived from those parameters. The modelling assumes LTE, but not optically thin emission. However, the fixed values of the source sizes and rotational temperatures make the fitted lines optically thin and the line profiles Gaussian. A Gaussian fit was performed to the CO (1–0) lines, but as it is highly affected by opacity, which affects the column density estimate, we did not include CO in our results and discussion. For the rest of the species, we fitted the molecules one by one, including in each case all the transitions along the observed frequency range (if there were more than one). As an exception, blended features were fitted simultaneously to take into account the contribution of each one to the total integrated areas.

The rotational temperature ($T_{\rm rot}$) of a given species can only be constrained if there are observations of several rotational

transitions. Additionally, if the molecule is faint, the error associated with its calculated $T_{\rm rot}$ could be by far larger than the value itself. As most of the species only have one transition in our survey, we fixed $T_{\rm rot}$ = 10 K. On average, as seen in our previous works, the rotational temperatures of the detected species are not expected to be much lower or higher than this value, although some exceptions are observed, such as seen for NH_2CN and CH_3CCH in NGC 253 and M 82 (Martín et al. 2006b; Aladro et al. 2011b), HC_3N and c-C_3H_2 in Arp 220 (Martín et al. 2011), and CN in Mrk 231 and Arp 220 (Henkel et al. 2014). The uncertainty added to the calculated column densities by assuming a fixed rotational temperature is not critical when comparing fractional abundances among galaxies; multi-line observations of many molecules in the nuclei of different galaxies and in the GC show that species also have very similar excitation conditions in different sources (e.g. Aladro et al. 2011b; Armijos-Abendaño et al. 2015). Thus the associated rotational temperature of a given molecule is expected (or measured) to be similar for all the galaxies of our sample, because the variations of $T_{\rm rot}$ are proportional to the differences in the gas temperature among sources. For this reason, comparing fractional abundances instead of column densities makes the analysis less sensitive to these changes.

In addition to the species mentioned before, there is the special case of the vibrationally excited lines of HC_3N, detected (only) in Arp 220. They are expected to trace gas with temperatures above 100 K (Costagliola & Aalto 2010; Martín et al. 2011). For these vibrational transitions, we calculated the temperature in a similar way as for the rotational temperatures and obtained $T_{\rm vib}$ = 190 ± 20 K.

Warm kinetic temperatures ($T_{\rm kin}$) estimated in the nuclear regions of these galaxies, such as 120 K for NGC 253 (Bradford et al. 2003) or ≥150 K for Mrk 231 (van der Werf et al. 2010), come from higher frequency observations and are only representative of a small fraction of the gas. Therefore, our assumption is still valid for the bulk of the molecular gas. Note, in any case, that rotational temperatures are lower than $T_{\rm kin}$, as the H_2 densities are below the critical densities. Previous extragalactic surveys also used similar assumptions, such as $T_{\rm rot}$ = 12 ± 6 K for NGC 253 (Martín et al. 2006b), 20 ± 10 K for M 82 (Aladro et al. 2011b), and 10 ± 5 K for NGC 1068 (Aladro et al. 2013).

5. Results

5.1. Summary of detections

In agreement with our previous surveys (Aladro et al. 2011b, 2013), we considered "detected" lines as those with a signal-to-noise ratio $S/N > 3$ and whose profiles can be clearly fitted by a Gaussian. Lines are considered "tentatively detected" when they have $1 < S/N \leq 3$, but can also be fitted with Gaussian profiles, whose velocities and line widths agree well with those obtained for detected lines (e.g. HC_5N lines, see Fig. 5). "Non-detected" lines are those with a $S/N \leq 1$ for which it is not possible to fit reliable Gaussian profiles, because the lines are dominated by the spectral noise.

Thirty-seven species (including isotopologues) were identified in NGC 253, which make it the most prolific galaxy of our sample in terms of molecular complexity. We detected the ^{13}C bearing isotopologues of CO, HCN, HCO^+, HNC, CN, and CS, the ^{18}O bearing isotopologues of CO and HCO^+, the ^{17}O isotopologue of CO, and the ^{34}S bearing isotopologue of CS. Furthermore, ^{13}CN, SO_2, NH_2CN, $HOCO^+$, HC_5N, H_2CS, and C_2S were only detected in NGC 253. Tables 2 and 3 list the total column densities of the thirty-six molecules and isotopologues in the eight galaxies (excluding CO, see Sect. 4.2). Molecules detected (tentatively or not) for the first time in each of the galaxies are marked in boldface.

Although tentative, this is the first time that HC_5N is detected outside the Milky Way. All the seven brighter transitions based on our synthetic spectra of HC_5N appear with measured intensities at 1−3σ level (see Table A.2, and Fig. 5). Deeper observations are needed to confirm this. We note, however, some inconsistencies in the identification of this species between Meier et al. (2015) and this work. The features that we identify as the HC_5N transitions ($J - J'$) = (33−31), (37−36), (38−37) at 87.8, 98.5, and 101.2 GHz respectively, were tentatively identified by Meier et al. (2015) as NH_2CHO, CH_3CH_2CN, and CH_3SH, also in the centre of NGC 253. We did not detect emission of these molecules in our survey, although we cannot rule out that this might be due to differences in sensitivity between the IRAM 30 m telescope and ALMA. However, we covered a broader range of frequencies where other HC_5N lines are also consistently detected, which makes us favour our identification. HC_5N was previously observed towards Galactic dense cores of dark clouds and seems to trace the initial conditions of star formation (e.g. Suzuki et al. 1992; Rathborne et al. 2008).

In addition, we found that c-C_3H_2, NS and, especially, CH_3CHO were detected in NGC 253 and M 82, but not in the rest of the galaxies of our sample. Outside the Milky Way, CH_3CHO was also tentatively detected in NGC 253 (Meier et al. 2015) and towards a galaxy at redshift z = 0.89 (Muller et al. 2011). Although little is known about this molecule, its origin seems to be linked to grain mantle destruction by shocks and is found in massive star-forming regions (e.g. Chengalur & Kanekar 2003; Bennett et al. 2005).

As commented in Sect. 4.3, we detected vibrationally excited lines of HC_3N only in Arp 220, which are listed in Table A.7. They trace the hottest and densest molecular gas in the inner regions of hot cores in star-forming regions (de Vicente et al. 2000; Martín-Pintado et al. 2005).

5.2. Column densities and fractional abundances

For the species that were not detected in a galaxy, we estimated the 3σ upper limit to the column density by assuming a limit to the integrated area (I) given by

$$I \leq 3 \times \mathrm{rms} \times \sqrt{FWHM \times D_{\rm v}}, \quad (2)$$

where rms is the 1σ noise level of the spectrum that contains the line, $D_{\rm v}$ is the spectral resolution in velocity units indicated in Sect. 3 for each galaxy, and FWHM is the average full width at half maximum of the Gaussian fits measured for other species in the same galaxy. As FWHM we generally used 95 km s^{-1} for M 83, 200 km s^{-1} for NGC 253, 100 km s^{-1} for M 82, 130 km s^{-1} for M 51, 240 kms^{-1} for NGC 1068, 250 km s^{-1} for NGC 7469, 390 km s^{-1} for Arp 220, and 210 km s^{-1} for Mrk 231. Note, however, that these values may differ for some species.

We calculated fractional abundances of all the species (or their upper limits when they were not detected) relative to the ^{12}C^{18}O (hereafter C^{18}O) column density, which is significantly less affected by opacity effects than the main oxygen isotopologue ^{12}C^{16}O. We note, however, that C^{18}O seems to be enhanced in the two ULIRGs of our sample. In Sect. 7.3, we discuss how this might affect our comparison of abundances among galaxies.

Table 2. Source-averaged column densities [cm^{-2}].

Molecule	M 83	NGC 253	M 82	M 51
^{13}CO	$(5.7 \pm 0.1) \times 10^{16}$	$(1.88 \pm 0.03) \times 10^{17}$	$(1.32 \pm 0.02) \times 10^{17}$	$(2.1 \pm 0.1) \times 10^{16}$
$C^{18}O$	$(1.10 \pm 0.03) \times 10^{16}$	$(5.1 \pm 0.2) \times 10^{16}$	$(2.61 \pm 0.08) \times 10^{16}$	$(5.2 \pm 0.4) \times 10^{15}$
$C^{17}O$	$(1.9 \pm 0.2) \times 10^{15}$	$(6.7 \pm 0.3) \times 10^{15}$	$(1.6 \pm 0.3) \times 10^{15}$	$(9.0 \pm 1.9) \times 10^{14}$
HCN	$(8.6 \pm 0.1) \times 10^{13}$	$(3.85 \pm 0.05) \times 10^{14}$	$(2.90 \pm 0.06) \times 10^{14}$	$(4.5 \pm 0.1) \times 10^{13}$
$H^{13}CN$	$\mathbf{(2.3 \pm 0.5) \times 10^{12}}$	$(2.8 \pm 0.1) \times 10^{13}$	$(5.0 \pm 0.6) \times 10^{12}$	$(1.8 \pm 0.4) \times 10^{12}$
HNC	$(3.13 \pm 0.09) \times 10^{13}$	$(1.81 \pm 0.02) \times 10^{14}$	$(1.16 \pm 0.03) \times 10^{14}$	$(1.35 \pm 0.06) \times 10^{13}$
$HN^{13}C$	$\mathbf{(1.2 \pm 0.6) \times 10^{12}}$	$(1.5 \pm 0.1) \times 10^{13}$	$\leq 2.1 \times 10^{12}$	$\leq 1.4 \times 10^{12}$
HCO^+	$(4.6 \pm 0.1) \times 10^{13}$	$(1.94 \pm 0.03) \times 10^{14}$	$(2.55 \pm 0.06) \times 10^{14}$	$(1.31 \pm 0.04) \times 10^{13}$
$H^{13}CO^+$	$\mathbf{(1.1 \pm 0.4) \times 10^{12}}$	$(1.3 \pm 0.2) \times 10^{13}$	$(6.9 \pm 0.3) \times 10^{12}$	$\leq 6.6 \times 10^{11}$
$HC^{18}O^+$	–	$(4.3 \pm 0.2) \times 10^{12}$	$(4.7 \pm 2.5) \times 10^{12}$	–
HOC^+	$\mathbf{(1.3 \pm 0.2) \times 10^{12}}$	$(6.4 \pm 0.4) \times 10^{12}$	$(3.6 \pm 0.2) \times 10^{12}$	$\leq 5.8 \times 10^{11}$
HCO	$\leq 5.0 \times 10^{12}$	$(5.9 \pm 0.2) \times 10^{13}$	$(5.1 \pm 0.6) \times 10^{13}$	$\leq 7.0 \times 10^{12}$
C_2H	$\mathbf{(5.0 \pm 0.1) \times 10^{14}}$	$(2.82 \pm 0.04) \times 10^{15}$	$(3.69 \pm 0.05) \times 10^{15}$	$(1.6 \pm 0.1) \times 10^{14}$
CN	$\mathbf{(3.24 \pm 0.04) \times 10^{14}}$	$(1.74 \pm 0.01) \times 10^{15}$	$(1.02 \pm 0.02) \times 10^{15}$	$(1.31 \pm 0.02) \times 10^{14}$
^{13}CN	$\leq 7.0 \times 10^{12}$	$(6.2 \pm 0.5) \times 10^{13}$	$\leq 1.2 \times 10^{13}$	$\leq 1.5 \times 10^{13}$
CH_3OH	$\mathbf{(1.9 \pm 0.2) \times 10^{14}}$	$(1.3 \pm 0.1) \times 10^{15}$	$(2.07 \pm 0.08) \times 10^{14}$	$(3.9 \pm 1.5) \times 10^{13}$
CS	$(5.7 \pm 0.1) \times 10^{13}$	$(4.07 \pm 0.07) \times 10^{14}$	$(2.50 \pm 0.05) \times 10^{14}$	$(1.8 \pm 0.1) \times 10^{13}$
$C^{34}S$	$(7.7 \pm 1.0) \times 10^{12}$	$(5.4 \pm 0.2) \times 10^{13}$	$(1.50 \pm 0.08) \times 10^{13}$	$(3.1 \pm 0.8) \times 10^{12}$
^{13}CS	$\leq 2.9 \times 10^{12}$	$(1.4 \pm 0.1) \times 10^{13}$	$\leq 4.6 \times 10^{12}$	$\leq 3.2 \times 10^{12}$
HC_3N	$\mathbf{(1.9 \pm 1.2) \times 10^{13}}$	$(1.04 \pm 0.05) \times 10^{14}$	$(4.6 \pm 0.4) \times 10^{13}$	$\leq 4.4 \times 10^{12}$
SO	$\mathbf{(2.0 \pm 0.3) \times 10^{13}}$	$(1.7 \pm 0.3) \times 10^{14}$	$(7.7 \pm 0.8) \times 10^{13}$	$(1.1 \pm 0.3) \times 10^{13}$
SO_2	$\leq 1.6 \times 10^{13}$	$(3.6 \pm 0.6) \times 10^{13}$	$\leq 2.0 \times 10^{13}$	$\leq 1.3 \times 10^{13}$
NS	$\leq 1.2 \times 10^{13}$	$(3.8 \pm 1.9) \times 10^{13}$	$(3.0 \pm 0.6) \times 10^{13}$	$\leq 6.4 \times 10^{12}$
HNCO	$(4.7 \pm 2.5) \times 10^{13}$	$(2.2 \pm 0.7) \times 10^{14}$	$\mathbf{(2.7 \pm 5.0) \times 10^{13}}$	$\leq 6.7 \times 10^{12}$
N_2H^+	$\mathbf{(6.5 \pm 0.3) \times 10^{12}}$	$(3.97 \pm 0.07) \times 10^{13}$	$(1.31 \pm 0.03) \times 10^{13}$	$(4.1 \pm 0.3) \times 10^{12}$
SiO	$\mathbf{(2.4 \pm 0.6) \times 10^{12}}$	$(3.1 \pm 0.3) \times 10^{13}$	$(4.4 \pm 0.6) \times 10^{12}$	$\leq 1.2 \times 10^{12}$
CH_3CN	$\mathbf{(3.4 \pm 0.9) \times 10^{12}}$	$(3.3 \pm 2.6) \times 10^{13}$	$(4.8 \pm 15.8) \times 10^{12}$	$\leq 1.8 \times 10^{12}$
CH_3CCH	$\mathbf{(9.4 \pm 5.7) \times 10^{13}}$	$(5.4 \pm 1.0) \times 10^{14}$	$(1.15 \pm 0.04) \times 10^{15}$	$\leq 5.3 \times 10^{13}$
c-C_3H_2	$\leq 3.7 \times 10^{15}$	$(1.05 \pm 0.06) \times 10^{14}$	$(1.31 \pm 0.06) \times 10^{14}$	$\leq 1.7 \times 10^{15}$
NH_2CN	$\leq 3.2 \times 10^{12}$	$(1.3 \pm 0.3) \times 10^{13}$	$\leq 3.9 \times 10^{12}$	$\leq 4.0 \times 10^{12}$
$HOCO^+$	$\leq 6.4 \times 10^{12}$	$(1.2 \pm 0.7) \times 10^{13}$	$\leq 6.1 \times 10^{12}$	$\leq 5.0 \times 10^{12}$
OCS	$\leq 7.3 \times 10^{13}$	$(4.9 \pm 0.3) \times 10^{14}$	$\leq 8.4 \times 10^{13}$	$\leq 7.4 \times 10^{13}$
C_2S	$\leq 7.6 \times 10^{12}$	$(2.5 \pm 0.8) \times 10^{13}$	$\leq 1.2 \times 10^{13}$	$\leq 1.9 \times 10^{13}$
H_2CS	$\leq 1.5 \times 10^{13}$	$(3.8 \pm 0.9) \times 10^{13}$	$\leq 1.4 \times 10^{13}$	$\leq 1.1 \times 10^{13}$
HC_5N	$\leq 3.5 \times 10^{14}$	$\mathbf{(7.1 \pm 13.4) \times 10^{13}}$	$\leq 3.8 \times 10^{14}$	$\leq 4.0 \times 10^{14}$
CH_3CHO	$\leq 1.1 \times 10^{13}$	$\mathbf{(7.4 \pm 64.7) \times 10^{13}}$	$\mathbf{(3.4 \pm 0.4) \times 10^{13}}$	$\leq 1.5 \times 10^{13}$

Notes. Molecules in boldface are new detections for a given galaxy. Column densities have been calculated for molecules clearly detected, and for those tentatively detected. Upper limits are shown for undetected species.

6. Key molecular species

Figure 6 shows the comparison of thirty-five molecular abundances among the eight galaxies in the sample. Table 4 lists the most relevant column density ratios used for the discussion in this section and the following. Based on these results, we indicate here the species presenting the highest abundance contrasts among our galaxy sample. These molecules are potentially good candidates for further high-resolution follow up observations. We note that we only discuss here species where the abundance difference is at least a factor of three.

– CH_3CCH is detected in M 83, NGC 253, M 82, and Arp 220, but not in the AGNs of our sample. M 82 has the highest CH_3CCH abundance and, in fact, no other galaxy has been found to have such a high value (at least relative to H_2, $C^{34}S$ and $C^{18}O$, Aladro et al. 2011a,b, 2013). The other galaxies where this species was detected have similar values, five to seven times lower than that of M 82. Interestingly, CH_3CCH was not detected in NGC 1068, NGC 7469, M 51, and Mrk 231, which supports the idea that this molecule is highly different in starbursts and AGNs (Aladro et al. 2013). The upper limits to the abundance of M 51 and NGC 1068 are significant and show that the difference in abundance between M 82 and NGC 1068 is about one order of magnitude.
In the Galaxy, CH_3CCH was found to be very abundant in regions of prolific star formation, where its column density is substantially higher ($N_{CH_3CCH} \sim 10^{14-15}\,cm^{-2}$, Churchwell & Hollis 1983; Miettinen et al. 2006), than in dark clouds, ($N_{CH_3CCH} \sim 10^{13}\,cm^{-2}$, Irvine et al. 1981; Markwick et al. 2005). Our values for M 82, M 83, NGC 253 and Arp 220 are of the same order as those cited above for high-mass star-forming cores. However, given the different scales in extragalactic and galactic sources, the comparison of the column densities is not straightforward. In addition, it was recently found that CH_3CCH is enhanced in PDRs in the Horsehead nebula as compared to dense cores (Guzmán et al. 2014). High temperatures could help to understand high abundances of CH_3CCH in these objects, because it may form after the desorption of its chemical precursors from grain mantles. In fact, rotational temperatures derived for Orion-KL, Sgr B2, DR 21 and many other similar sources are in the range [20−50] K (Churchwell & Hollis 1983; Miettinen et al. 2006).

Table 3. Source-averaged column densities [cm^{-2}].

Molecule	NGC 1068	NGC 7469	Arp 220	Mrk 231
^{13}CO	$(4.6 \pm 0.1) \times 10^{17}$	$(3.6 \pm 0.2) \times 10^{16}$	$(6.6 \pm 0.4) \times 10^{17}$	$(5.6 \pm 0.9) \times 10^{16}$
$C^{18}O$	$(1.29 \pm 0.04) \times 10^{17}$	$(6.4 \pm 1.3) \times 10^{15}$	$(6.2 \pm 0.4) \times 10^{17}$	$(4.9 \pm 0.9) \times 10^{16}$
$C^{17}O$	$\leq 1.0 \times 10^{16}$	$\leq 3.9 \times 10^{15}$	$\leq 2.9 \times 10^{16}$	$\leq 2.2 \times 10^{16}$
HCN	$(2.45 \pm 0.04) \times 10^{15}$	$(1.04 \pm 0.08) \times 10^{14}$	$(4.6 \pm 0.1) \times 10^{15}$	$(8.5 \pm 0.7) \times 10^{14}$
$H^{13}CN$	$(8.1 \pm 0.8) \times 10^{13}$	$\leq 1.4 \times 10^{13}$	$\mathbf{(7.1 \pm 0.5) \times 10^{14}}$	$(2.0 \pm 0.5) \times 10^{14}$
HNC	$(7.0 \pm 0.1) \times 10^{14}$	$(4.2 \pm 0.5) \times 10^{13}$	$(3.2 \pm 0.2) \times 10^{15}$	$(2.5 \pm 0.7) \times 10^{14}$
$HN^{13}C$	$(2.4 \pm 0.6) \times 10^{13}$	$\leq 1.6 \times 10^{13}$	$\leq 1.3 \times 10^{14}$	$\leq 1.8 \times 10^{14}$
HCO^+	$(9.1 \pm 0.2) \times 10^{14}$	$(7.4 \pm 0.5) \times 10^{13}$	$(1.12 \pm 0.06) \times 10^{15}$	$(3.3 \pm 0.3) \times 10^{14}$
$H^{13}CO^+$	$\leq 9.0 \times 10^{12}$	$\leq 8.0 \times 10^{12}$	$(9.8 \pm 3.2) \times 10^{13}$	$\leq 9.1 \times 10^{13}$
$HC^{18}O^+$	–	–	–	–
HOC^+	$(1.6 \pm 0.4) \times 10^{13}$	$\leq 6.8 \times 10^{12}$	$\leq 5.6 \times 10^{13}$	$\leq 6.2 \times 10^{13}$
HCO	$(2.6 \pm 0.8) \times 10^{14}$	$\leq 7.1 \times 10^{13}$	$\leq 5.7 \times 10^{14}$	$\leq 8.0 \times 10^{14}$
C_2H	$(1.10 \pm 0.02) \times 10^{16}$	$(1.0 \pm 0.1) \times 10^{15}$	$\mathbf{(2.2 \pm 0.1) \times 10^{16}}$	$(3.4 \pm 0.7) \times 10^{15}$
CN	$(6.85 \pm 0.06) \times 10^{15}$	$(4.6 \pm 0.2) \times 10^{14}$	$(6.1 \pm 0.2) \times 10^{15}$	$(1.8 \pm 0.1) \times 10^{15}$
^{13}CN	$\leq 1.5 \times 10^{14}$	$\leq 6.6 \times 10^{13}$	$\leq 5.8 \times 10^{14}$	$\leq 1.4 \times 10^{14}$
CH_3OH	$(2.4 \pm 0.2) \times 10^{15}$	$\leq 1.8 \times 10^{14}$	$(5.6 \pm 0.6) \times 10^{15}$	$\leq 2.6 \times 10^{15}$
CS	$(7.6 \pm 0.2) \times 10^{14}$	$(8.1 \pm 1.0) \times 10^{13}$	$(3.36 \pm 0.08) \times 10^{15}$	$(3.5 \pm 0.8) \times 10^{14}$
$C^{34}S$	$(1.3 \pm 0.2) \times 10^{14}$	$\leq 3.0 \times 10^{13}$	$(9.6 \pm 1.3) \times 10^{14}$	$\leq 2.3 \times 10^{14}$
^{13}CS	$\leq 3.6 \times 10^{13}$	$\leq 3.0 \times 10^{13}$	$\leq 2.0 \times 10^{14}$	$\leq 2.0 \times 10^{14}$
HC_3N	$(1.50 \pm 0.07) \times 10^{14}$	$\leq 5.0 \times 10^{13}$	$(2.7 \pm 0.2) \times 10^{15}$	$(2.1 \pm 0.5) \times 10^{14}$
SO	$(2.2 \pm 0.4) \times 10^{14}$	$\leq 6.9 \times 10^{13}$	$\leq 4.4 \times 10^{14}$	$\leq 5.0 \times 10^{14}$
SO_2	$\leq 7.4 \times 10^{15}$	$\leq 1.1 \times 10^{14}$	$\leq 9.2 \times 10^{14}$	$\leq 1.1 \times 10^{15}$
NS	$\leq 9.6 \times 10^{13}$	$\leq 8.0 \times 10^{13}$	$\leq 3.1 \times 10^{14}$	$\leq 5.5 \times 10^{14}$
HNCO	$(3.2 \pm 0.4) \times 10^{14}$	$\leq 6.0 \times 10^{13}$	$(1.8 \pm 0.9) \times 10^{15}$	$\leq 3.0 \times 10^{14}$
N_2H^+	$(1.2 \pm 0.5) \times 10^{14}$	$\leq 8.2 \times 10^{12}$	$(5.9 \pm 0.3) \times 10^{14}$	$\leq 5.4 \times 10^{13}$
SiO	$(6.8 \pm 0.8) \times 10^{13}$	$\leq 1.5 \times 10^{13}$	$(6.3 \pm 0.7) \times 10^{14}$	$\leq 1.7 \times 10^{14}$
CH_3CN	$(1.0 \pm 2.9) \times 10^{14}$	$\leq 1.7 \times 10^{13}$	$(9.2 \pm 1.7) \times 10^{14}$	$\leq 9.1 \times 10^{13}$
CH_3CCH	$\leq 5.7 \times 10^{14}$	$\leq 3.7 \times 10^{14}$	$(3.7 \pm 0.8) \times 10^{15}$	$\leq 4.0 \times 10^{15}$
c-C_3H_2	$\leq 2.7 \times 10^{16}$	$\leq 3.9 \times 10^{15}$	$\leq 4.4 \times 10^{16}$	$\leq 5.3 \times 10^{14}$
NH_2CN	$\leq 2.6 \times 10^{13}$	$\leq 2.2 \times 10^{13}$	$\leq 1.5 \times 10^{14}$	$\leq 1.8 \times 10^{14}$
$HOCO^+$	$\leq 7.7 \times 10^{13}$	$\leq 4.4 \times 10^{13}$	$\leq 3.7 \times 10^{14}$	$\leq 3.5 \times 10^{14}$
OCS	$\leq 8.9 \times 10^{14}$	$\leq 8.2 \times 10^{14}$	$\leq 6.1 \times 10^{15}$	$\leq 9.2 \times 10^{15}$
C_2S	$\leq 1.2 \times 10^{14}$	$\leq 9.3 \times 10^{13}$	$\leq 6.5 \times 10^{14}$	$\leq 7.1 \times 10^{14}$
H_2CS	$\leq 1.6 \times 10^{14}$	$\leq 9.0 \times 10^{13}$	$\leq 6.6 \times 10^{14}$	$\leq 7.6 \times 10^{14}$
HC_5N	$\leq 5.4 \times 10^{15}$	$\leq 4.9 \times 10^{15}$	$\leq 4.0 \times 10^{16}$	$\leq 3.9 \times 10^{16}$
CH_3CHO	$\leq 4.6 \times 10^{14}$	$\leq 1.2 \times 10^{14}$	$\leq 7.2 \times 10^{14}$	$\leq 1.3 \times 10^{15}$

Notes. Molecules in boldface are new detections in a given galaxy. Column densities have been calculated for molecules clearly detected, and for those tentatively detected. Upper limits are shown for undetected species.

Table 4. Relevant column density ratios used for the discussion.

Molecular ratio	M 83	NGC 253	M 82	M 51	NGC 1068	NGC 7469	Arp 220	Mrk 231
$HNCO/C^{18}O$	4.3×10^{-3}	4.3×10^{-3}	1.0×10^{-3}	$\leq 1.3 \times 10^{-3}$	2.5×10^{-3}	$\leq 9.4 \times 10^{-3}$	2.9×10^{-3}	$\leq 6.1 \times 10^{-3}$
$CH_3OH/C^{18}O$	1.7×10^{-2}	2.5×10^{-2}	7.9×10^{-3}	7.5×10^{-3}	1.9×10^{-2}	$\leq 2.8 \times 10^{-2}$	9.0×10^{-3}	$\leq 5.3 \times 10^{-2}$
$SiO/C^{18}O$	2.2×10^{-4}	6.1×10^{-4}	1.7×10^{-4}	$\leq 5.0 \times 10^{-5}$	5.3×10^{-3}	$\leq 2.3 \times 10^{-3}$	1.1×10^{-3}	$\leq 3.5 \times 10^{-3}$
$CH_3CN/C^{18}O$	3.1×10^{-4}	6.5×10^{-4}	1.8×10^{-4}	$\leq 1.8 \times 10^{-3}$	7.8×10^{-4}	$\leq 2.6 \times 10^{-3}$	1.5×10^{-3}	$\leq 1.8 \times 10^{-3}$
$CH_3CCH/C^{18}O$	8.5×10^{-3}	1.0×10^{-2}	4.4×10^{-2}	$\leq 1.0 \times 10^{-2}$	$\leq 4.4 \times 10^{-3}$	$\leq 5.8 \times 10^{-2}$	6.0×10^{-3}	$\leq 8.2 \times 10^{-2}$
$SO/C^{18}O$	1.8×10^{-3}	3.3×10^{-3}	3.0×10^{-3}	2.1×10^{-3}	1.7×10^{-3}	$\leq 1.1 \times 10^{-2}$	$\leq 7.1 \times 10^{-4}$	$\leq 1.0 \times 10^{-2}$
c-$C_3H_2/C^{18}O$	$\leq 3.4 \times 10^{-1}$	2.0×10^{-3}	5.1×10^{-3}	$\leq 3.3 \times 10^{-1}$	$\leq 2.1 \times 10^{-1}$	$\leq 6.1 \times 10^{-1}$	$\leq 7.1 \times 10^{-2}$	$\leq 1.1 \times 10^{-2}$
$HCO/C^{18}O$	$\leq 4.5 \times 10^{-4}$	1.2×10^{-3}	2.0×10^{-3}	$\leq 1.3 \times 10^{-3}$	2.0×10^{-3}	$\leq 1.1 \times 10^{-2}$	$\leq 9.2 \times 10^{-4}$	$\leq 1.6 \times 10^{-2}$
$C_2H/C^{18}O$	4.5×10^{-2}	5.5×10^{-2}	1.4×10^{-1}	3.1×10^{-2}	8.5×10^{-2}	1.6×10^{-1}	3.5×10^{-2}	6.9×10^{-2}
$N_2H^+/C^{18}O$	5.9×10^{-4}	7.8×10^{-4}	5.1×10^{-4}	7.9×10^{-4}	2.5×10^{-3}	$\leq 1.3 \times 10^{-3}$	9.5×10^{-4}	$\leq 1.1 \times 10^{-3}$
$HNC/C^{18}O$	2.8×10^{-3}	3.5×10^{-3}	4.4×10^{-3}	2.6×10^{-3}	5.4×10^{-3}	6.6×10^{-3}	5.2×10^{-3}	5.1×10^{-3}
$HCN/C^{18}O$	7.8×10^{-3}	7.5×10^{-3}	1.1×10^{-2}	8.6×10^{-3}	1.9×10^{-2}	1.6×10^{-2}	7.4×10^{-3}	1.7×10^{-2}
$CN/C^{18}O$	2.9×10^{-2}	3.4×10^{-2}	3.9×10^{-2}	2.5×10^{-2}	5.3×10^{-2}	7.2×10^{-2}	9.8×10^{-3}	3.7×10^{-2}
HCN/HCO^+	1.9	2.0	1.1	3.4	2.7	1.4	4.1	2.6
CN/HCN	3.8	4.5	3.5	2.9	2.8	4.4	1.3	2.1
HCN/CS	1.5	0.9	1.2	2.5	3.2	1.3	1.4	2.4

Notes. The errors of the ratios range in general between 2% and 63% and have an average value of 14%. Exceptions to these values are the ratios involving HNCO and CH_3CN in M 82, as their column densities have large errors associated.

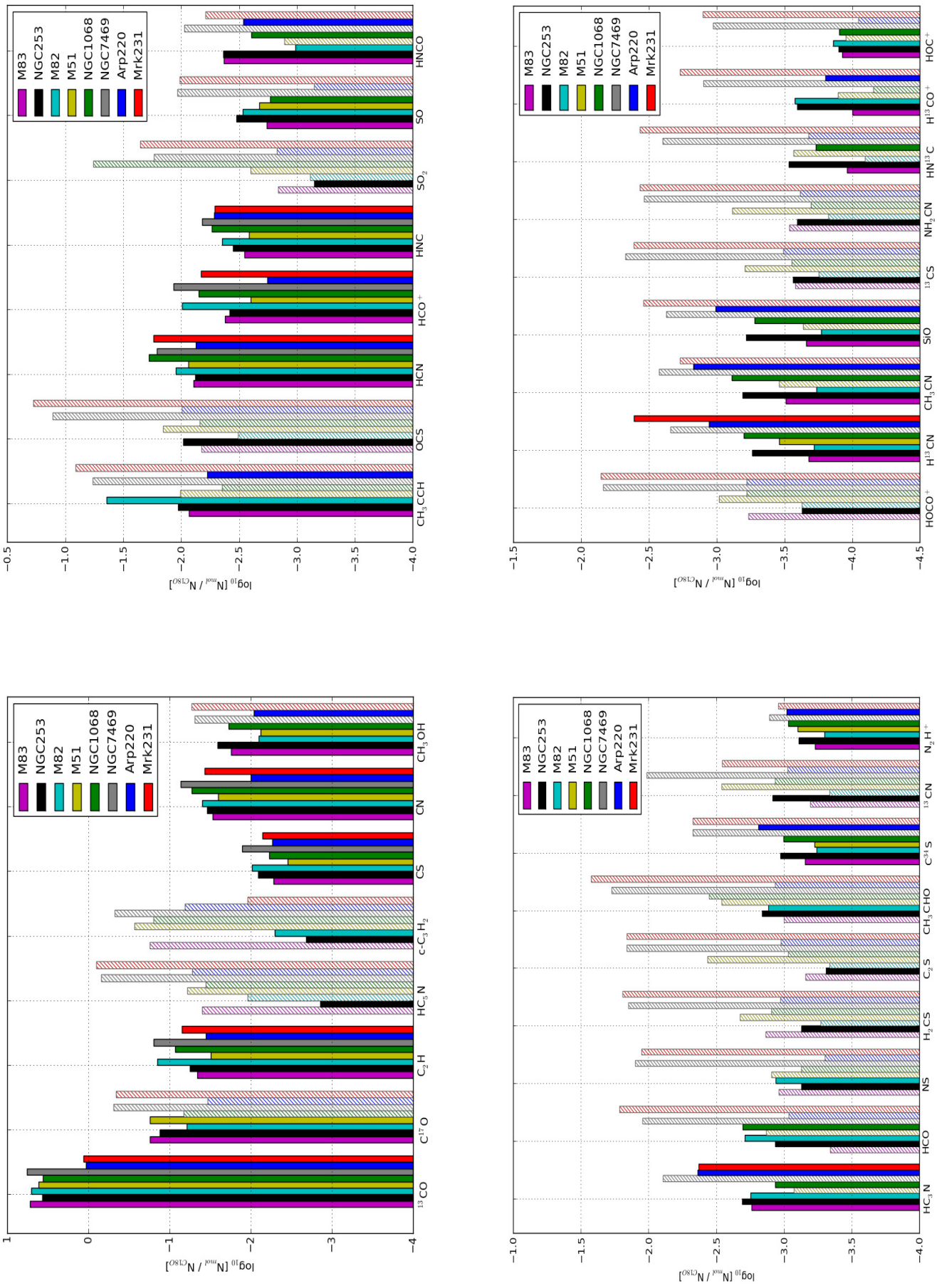

Fig. 6. Abundances of 34 species relative to $C^{18}O$ for the eight galaxies of our sample. Dashed histograms indicate upper limits.

As previously claimed by Aladro et al. (2013) and in agreement with our results here, the abundance of CH_3CCH seems to be enhanced in starburst galaxies. It is a known tracer of relatively dense gas (the critical densities for the two transitions observed here are 10^4–10^5 cm^{-3}). Its emission is more widespread than that of other similar molecules, such as CH_3CN, and can also be found in regions outside the cores of the molecular clouds (Aladro et al. 2011a). The response of CH_3CCH to the presence of UV fields and shocks has not been studied in detail in extragalactic sources. Consequently, the chemistry of CH_3CCH is still uncertain, but it might well be that the paths for its production are more effective in the presence of UV radiation fields created by massive star formation (see Aladro et al. 2011b, and references therein). Supporting this idea, recent interferometric maps of several species in the central half kiloparsec of NGC 253 show that the emission of CH_3CCH has a similar morphology to other PDR tracers, such as C_2H (Meier et al. 2015). Thus, it seems that, apart from being a dense gas tracer, CH_3CCH can also be considered a PDR tracer.

– HC_3N and $H^{13}CN$ show clearly enhanced abundances in Arp 220 and Mrk 231 with respect to the rest of galaxies in our sample. This could be related to larger amounts of dense gas and warm dust present in ULIRGs (as compared to less obscured galaxies, Lindberg et al. 2011), where the dust would prevent their photo-dissociation. On average, the differences between the ULIRGs and the other galaxies is a factor of three for HC_3N and seven for $H^{13}CN$, although the strongest differences between individual galaxies are of factors four and twenty-one for HC_3N and $H^{13}CN$ respectively.
– CH_3CN and SiO have the highest abundances in Arp 220, where they are a factor of 7 larger than those of M 82, which shows the minimum in both cases. Both species are found to be tracers of dense gas and shocks, although enhanced SiO abundances may also be related to X-ray chemistry in AGNs (García-Burillo et al. 2010; Aladro et al. 2013). The species are photo-dissociated in the external layers of molecular clouds if strong UV fields are present. This scenario agrees with both molecules having high abundances in Arp 220, which probably has more dense gas and dust, and a minimum in M 82, because it is heavily pervaded by UV fields.
– Previous observational studies found high abundances of C_2H in PDRs of starburst galaxies (e.g. Meier & Turner 2005; Fuente et al. 2005; Aladro et al. 2011b). Together with M 82, the highest abundances of C_2H in our sample are also those of NGC 7469 and NGC 1068, while M 51 presents the lowest value, followed by Arp 220 and M 83. There is a factor five of difference between the abundances of M 82 and M 51. For NGC 1068 and NGC 7469, significant emission probably arises from the circumnuclear star forming rings, as in NGC 1097 (Martín et al. 2015).
– CN and HCN abundances stand out in NGC 7469, NGC 1068, Mrk 231, and M 82, with the difference between these galaxies and the rest of the sample larger in HCN. In agreement with previous observations (e.g. Aalto et al. 2002; Aalto 2008) and model predictions (Lepp & Dalgarno 1996; Sternberg & Dalgarno 1995; Meijerink & Spaans 2005), our data indicate that CN and HCN could be effectively produced in the X-ray and UV-field dominated regions expected in AGN and starburst galaxies.
– HNCO is tentatively detected for the first time in M 82. This species is claimed to be a good indicator of the evolution of nuclear starbursts in galaxies, with abundances decreasing toward the last evolutionary stages of the starbursts (in those late phases HNCO is expected to be efficiently destroyed by means of reactions involving the abundant UV photons and/or ions). HNCO remained undetected in previous studies of M 82 (Martín et al. 2009a; Aladro et al. 2011b). Our new tentative HNCO line detections in M 82 have intensities of ∼3 mK, which are higher than the upper limit of <1.3 mK previously estimated by Martín et al. (2009a). Our HNCO abundances in M 82 are four times lower than in NGC 253 and M 83. This contrast is lower than that found by Martín et al. (2009a) for HNCO/$C^{34}S$, which shows differences of nearly two orders of magnitude, but goes in the same direction. Therefore, our observations agree with HNCO being a good tracer of the evolutionary stage of starburst galaxies.
– $C^{32}S/C^{34}S$. Both ^{32}S and ^{34}S are believed to be a product of hydrostatic or explosive oxygen-burning in massive stars and Type Ia supernovae (see Chin et al. 1996 and references therein). However, not much is known apart from some Galactic observations that indicate that $^{32}S/^{34}S$ increases with the galactocentric radius (Chin et al. 1996). In external galaxies, more data are needed to know how this ratio varies from source to source.
We found that the $C^{32}S$ (2−1)/$C^{34}S$ (2−1) line ratio is five times higher in M 82 (with the highest value of 21.5 in our sample) than in Arp 220 (lowest value of 4.5, similar to that derived with SO by Martín et al. 2011). This points to a higher CS opacity in Arp 220 where there is much more molecular gas. As a reference value, $C^{32}S/C^{34}S$ in the Galactic centre (GC), the local ISM, and the solar system is ∼22, (Frerking et al. 1980). M 82 has a similar value to the GC, which is about three times higher than that of NGC 253 (7.6). More sophisticated estimates by Martín et al. (2010) and Henkel et al. (2014) give values close to the local interstellar value for NGC 253 (>16).
NGC 1068, M 51, NGC 253, and M 83 have $C^{32}S/C^{34}S$ $J = 2 \rightarrow 1$ line ratios of 6−8, well below the GC and M 82, and closer to the value in Arp 220. Although these ratios indicate the degree of processing of the ISM in the galactic nuclei, the values should be taken with care, because opacity on the main isotopologue might play an important role in these regions (Martín et al. 2010; Henkel et al. 2014, and references therein). Opacity becomes less of an issue for LIRGs, based on the $^{13}CO/C^{18}O$ sample measured by Costagliola et al. (2011).

7. Chemical caracterisation of our sample

7.1. Starburst galaxies

The molecular gas in the nuclear region of M 83 is rich in some shock tracers and species formed in dust grains, such as HNCO and CH_3OH (Fig. 6 and Table 4), which are easily released through grain-mantle evaporation by shock waves. Although the abundances of these two species are high relative to $C^{18}O$ (10^{-3} and 10^{-2} for HNCO and CH_3OH, respectively), other shock and dense gas tracers are just marginally detected (e.g. SiO, CH_3CN, and SO). No Hα recombination lines were detected in M 83, unlike in the more active starbursts (see SFR in Table 1) M 82 and NGC 253, even though all three galaxies have similar beam-filling factors. This suggests that extended and medium-size HII regions and OB star clusters are relatively scarce in M 83. Accordingly, the PDR-tracers c-C_3H_2 and HCO were not detected.

As for NGC 253, groups of OB stars create photo-dissociated regions in the outskirts of the molecular clouds. This is confirmed by previous detections of PDR tracers, such as HOC^+, CO^+, HCO, and c-C_3H_2 (Martín et al. 2009b), which are easily formed by ion-molecule reactions in gas phase (e.g. Hollis & Churchwell 1983; Thaddeus et al. 1985). However, the gas in NGC 253 is mainly characterised by the presence of many shock tracers and species formed in the icy mantles of dust grains. HNCO, CH_3OH, and SO are a factor of two more abundant than in M 83. Some other faint shock tracers have only been detected in this galaxy, such as $HOCO^+$ and NS, as well as the sulphur bearing species SO_2. H_2CS, and C_2S (Martín et al. 2003, 2005) which are confirmed here (see Fig. 6).

The gas in the NE lobe of M 82 is strongly affected by UV fields that shape its chemical composition (e.g. Aladro et al. 2011b). Molecular clouds are highly ionized and fragmented (Fuente et al. 2008) and, according to our results, the PDR tracers c-C_3H_2, HCO, and HOC^+ have slightly higher abundances than in NGC 253 (but just a factor of two or less. See Table 4). The species that shows the largest difference between M 82 and the other two starburst galaxies is CH_3CCH; it is five times more abundant in the former (see Sect. 6 for more details). Still, some shock tracers, such as CH_3OH, SiO, and HNCO, are detectable in the cores of the molecular clouds that are well shielded from the UV radiation (Martín et al. 2006a). However, their abundances are four times lower than in NGC 253, indicating that, although present, shocks do not represent the main heating mechanism of the molecular gas as compared to UV radiation.

7.1.1. Possible chemical scenario of starburst evolution

As commented in Sect. 2, M 83, NGC 253, and M 82 can be taken as examples of starbursts in an early, intermediate, and late stage of evolution. If this holds true, it may be possible to link their evolutionary stages to the chemical composition of their molecular gas. This evolutionary scenario has been progressively fine-tuned by several authors (García-Burillo et al. 2002; Martín et al. 2006b; Aladro et al. 2011b). An early starburst is expected to be chemically characterised by the absence of most PDR tracers (HCO, c-C_3H_2) and Hα recombination lines, as well as the presence of only the most common shock-tracers (HNCO, CH_3OH, SiO). Physically, first shocks might be caused by close encounters or mergers between galaxies, or by collisions of giant molecular cloud complexes (for example, following the bar potential toward the centre of the galaxy, Binney et al. 1991).

In an intermediate starburst stage, with similar characteristics to NGC 253, the stellar population would contain more recently formed young massive stars and supernovae events that ionise the outer layers of the molecular clouds, as seen by the detection of the PDR tracers c-C_3H_2, HCO and HOC^+. During this phase, PDR tracer abundance enhancements are still smaller than those caused by shocks, which would reach their strongest influence over the ISM at this point. Molecules such as CH_3OH, HNCO, and SO have higher abundances than in a previous (and later) phase. Other shock tracers would be also detectable, specifically $HOCO^+$ and some sulphur-bearing species, such as H_2CS, OCS, SO, SO_2 and C_2S (see Martín et al. 2003, 2005 and Fig. 6), whose abundances are enhanced during the last evolutionary stages of hot cores.

Finally, an advanced starburst such as that found in M 82 would be characterised by super-winds created by massive stars and supernovae, as well as a larger population of high-mass X-ray binaries, which provide a modest X-ray emission, needed to understand the abundance of some molecular species, such as CO^+ (Spaans & Meijerink 2007; Chiang & Kong 2011). Stellar winds enrich the ISM with both PDR tracers (HCO, HOC^+, c-C_3H_2, and CH_3CCH) and shock-tracers (CH_3OH, SiO, OCS, SO), the first ones being more abundant, since UV fields are more intense than in previous stages. Less abundant, or more complex, shock tracers and sulphur species would be easily photo-dissociated by the radiation fields, and thus would become less abundant than in previous starburst phases or not detectable at all.

7.2. Seyfert galaxies

Among the galaxies in our sample, M 51, NGC 1068, and NGC 7469 host an AGN (the first two are classified as Sy 2, and the latter as Sy 1, Osterbrock & Martel 1993). A detailed study devoted to our results in NGC 1068 has been presented by Aladro et al. (2013). The CNDs of these galaxies are surrounded by arms of active star-forming regions at ~1−2 kpc distance from their centres. Given the angular resolution of the IRAM 30 m telescope at 3 mm wavelengths (22″−29″), our data embrace the CNDs as well as the surrounding regions, so some contribution from the star-forming rings is expected in our data. Other observations of NGC 1068 indicate that some molecules show significant emission from the starburst ring (<25% for SiO (2−1) and <30% for HCO^+(1−0), Usero et al. 2004), while high transitions of the dense gas tracers HCN, HCO^+ and CS are hardly detected outside the CND (García-Burillo et al. 2014). Recently, Takajima et al. (in prep.) carried out a similar molecular line survey of NGC 1068 with the Nobeyama 45 m telescope. Thanks to the smaller beam size of that telescope at λ = 3 mm, their observations were able to separate the emission of the CND and that of the starburst ring and showed that the emission of some species such as C_2H and N_2H^+ come mainly from the latter. Unfortunately, there are no similar estimations for NGC 7469 and M 51 calculated for the IRAM 30 m beam at the 3 mm wavelength of our survey.

CH_3CCH and c-C_3H_2 were not detected in any of the AGNs, while HCO and HOC^+ are only tentatively seen in NGC 1068 and have similar abundances than in the starburst galaxies. Regarding shocks and dust grain chemistry, most of the tracers (such as OCS, HNCO, or SO) are only detected in NGC 1068. Shocks seem to be affecting part of the gas in the CND of this galaxy (Krips et al. 2011; Viti et al. 2014). CH_3OH is also detected in M 51 (not in NGC 7469), but with a clearly lower abundance than in NGC 1068.

Among others, we examined the following relative abundances: HCN/$C^{18}O$, CN/$C^{18}O$, HCN/HCO^+, CN/HCN, and HCN/CS (Table 4). The last three were proposed as discriminators between AGNs and starburst activities based on two-dimensional plots of line ratios (Kohno et al. 2001; Meijerink et al. 2007; Krips et al. 2008; Izumi et al. 2013). According to our data, HCN/CS, HCO^+/HCN, and CN/HCN, either by themselves and plotting one ratio versus other, do not show a correlation with the galactic nuclear activity of our sample. The most probable reason for the lack of trend between all these line ratios and AGNs (versus starburst galaxies) is the low angular resolution of the IRAM 30 m telescope, which is insufficient to separate the CND and the surrounding starburst regions. However, we do see that the HCN abundance is clearly enhanced in AGNs, and the reason for this might be a high temperature-driven chemistry (Izumi et al. 2013), or shocked regions at a few hundred parsecs from the super massive black holes due to outflowing material (Martín et al. 2015). Interestingly, HCN/$C^{18}O$, CN/$C^{18}O$,

$C_2H/C^{18}O$, and $HNC/C^{18}O$ in M 51 are closer to the starburst results than to the other AGNs (Fig. 6).

SiO is tentatively detected in NGC 1068, but not in M 51 and NGC 7469. For NGC 7469, where lines are weaker, we cannot conclude from the upper limit to the SiO abundance whether the gas chemistry is different. This species usually traces shocks in Galactic and extragalactic sources (Martín-Pintado et al. 1992, 1997; García-Burillo et al. 2000, 2001; Riquelme et al. 2010; Takano et al. 2014). However, some studies (based on observational data or on chemical models) indicate thar SiO is a tracer of X-rays and cosmic rays in the centres of the Milky Way and NGC 1068 (Martín-Pintado et al. 2000; Usero et al. 2004; Aladro et al. 2013). If that is the case in all AGNs, its detection in the other two Seyfert galaxies of our sample would be somehow expected (if SiO were strong enough to be detectable). A study devoted to this molecule is necessary to better understand how it is formed under the different regimes (i.e. shock-dominated versus X-ray dominated gas).

Using the IRAM 30 m telescope, Watanabe et al. (2014) carried out a molecular line survey in the 3 mm and 2 mm bands outside the nucleus of M 51. They observed two regions in a spiral arm of the galaxy. Their position P1 has twice the SFR of position P2. Both SFRs are quite low, in the range [0.02−0.05] $M_\odot\,yr^{-1}$. This allows us, for the first time, to compare the nuclear molecular gas composition with that outside the central region. Comparing the fractional abundances (with respect to $C^{18}O$) of the 22 species in common between our work and Watanabe's, we find that the chemical composition of the gas is fairly similar, except for a few cases. $H^{13}CO^+$, HNCO, and c-C_3H_2 are detected in the P1 position, but not in the centre. On the other hand, we detect $H^{13}CN$, $C^{34}S$, and SO, which are not seen in the P2 position. Apart from that, the rest of the molecules have similar abundances, within a factor of <2 in the three positions. One would expect that the chemistry of the gas might change between the nucleus, affected by higher star formation and the proximity of the black hole, and the spiral arms. However, given the beam size of the IRAM 30 m at these frequencies and the source sizes of the three positions, the emission might be so diluted that the differences are cancelled out. Further investigations with interferometers are needed to better understand the change of the gas chemistry as a function of galactocentric radius.

7.3. ULIRGs

Independently of their powering source, the ULIRGs of our sample show some chemical differences with respect to the AGNs and starburst galaxies described in the previous sections, as well as some dissimilarities between Arp 220 and Mrk 231 themselves.

The HNC (1−0) line intensity in Arp 220 slightly exceeds that of HCN (1−0) by a factor of 1.3, while for Mrk 231 we obtain HNC/HCN (1−0) = 0.6. This particularly high ratio in Arp 220 was already noted by Huettemeister et al. (1995) and Aalto et al. (2007) and seems to be due to an overabundance of HNC in this galaxy, a consequence of either mid-IR pumping of the lines or a chemistry driven by X-ray dominated regions (Meijerink et al. 2007; Aalto et al. 2007). A priori, we cannot rule out any of the two scenarios with our data, since we would need several HCN and HNC transitions to estimate the H_2 column and volume densities, which is indispensable to address the situation. However, we dare to favour IR pumping effects, given that the chemical composition of Arp 220 is not similar to the AGNs of our sample (XDR scenario), as we describe below.

CH_3CN and SiO are relatively abundant in Arp 220 (few $\times10^{-3}$ with respect to $C^{18}O$), but are not detected in Mrk 231. On the other hand, HCO^+, $H^{13}CN$, and CN are four times more abundant in Mrk 231 than in Arp 220. Our results suggest that the Arp 220 chemistry resembles the starburst galaxies of our sample dominated by shocks more closely, with high abundances of HC_3N, CH_3OH, HNCO, CH_3CN and SiO relative to $C^{18}O$ ($10^{-2,-3}$), but no PDR tracer detections (c-C_3H_2, HCO, HOC^+), except for CH_3CCH (just tentatively detected). This would support the infrared pumping of HNC in the galaxy at the expense of a XDR environment, as mentioned before. Mrk 231, in contrast, is characterised by high abundances of CN, HCN and $H^{13}CN$ relative to $C^{18}O$ ($10^{-2,-3}$), more similar to those found in NGC 1068 and NGC 7469.

Vibrationally excited lines from HC_3N, arising from dense ($n \geq 10^6\,cm^{-3}$) and hot ($T_{ex} = 190 \pm 20$ K) cores, are detected in Arp 220. They are a factor 4−5 fainter than the corresponding rotational transitions. Assuming that this ratio may be similar for the rest of the galaxies, the expected vibrational intensities in Mrk 231 would be ~0.2 mK, which is well below our rms level. Thus, we cannot discard lower level vibrational emission in Mrk 231. However, vibrationally excited HC_3N lines would be observable in NGC 253 and M 82, but are not detected. This clearly points to a different excitation between normal starbursts and ULIRGs.

There are also common features between the Mrk 231 and Arp 220 spectra as compared to the rest of the sample. In agreement with previous studies (Greve et al. 2009; Martín et al. 2011; Henkel et al. 2014) ^{13}CO and $C^{18}O$ are equally abundant in both ULIRGs. This may be due to high opacities of the ^{13}CO lines, to an intrinsic underabundance of ^{13}CO in luminous infrared galaxies (Taniguchi et al. 1999), or/and to a $C^{18}O$ overabundance due to the strong starbursts (Matsushita et al. 2009; Martín et al. 2011). High opacities of ^{13}CO in these two galaxies seem unlikely, given the weakness of the $^{13}CO(1-0)$ lines relative to $^{12}CO(1-0)$ (they are ≥20 times fainter). An overabundance of ^{18}O in Arp 220 has recently been found by González-Alfonso et al. (2014). However, the $^{12}C/^{13}C$ and $^{16}O/^{18}O$ line ratios obtained for Arp 220 and Mrk 231 by Henkel et al. (2014) do not favour this last scenario. It can be seen in Fig. 6 that the $^{13}CO/C^{18}O$ ratios in Mrk 231 and Arp 220 are a factor of about four lower than in the rest of the galaxies. We obtain a $^{12}CO/^{13}CO$ (1−0) relative intensity of 21 ± 7, which is a factor two lower than that obtained by Greve et al. (2009) for Arp 200 (43 ± 10). We note that our ^{12}CO (1−0) and ^{13}CO (1−0) lines were observed simultaneously with the EMIR receiver of the 30 m telescope, while Greve et al. (2009) used older data to derive this ratio, which may be less accurate.

In addition, $HC_3N/C^{18}O$ ratios are clearly higher in the ULIRGs than in the more nearby starbursts and AGNs observed by us. If $C^{18}O$ is overabundant in ULIRGs, then HC_3N should be it as well. This effect was already observed in other LIRGs/ULIRGs, and the reason could be a higher amount of dense gas and warm dust that protects the species from being photo-dissociated (Aalto et al. 2007; Costagliola et al. 2011; Lindberg et al. 2011). Thus, HC_3N seems to be a well-suited species for studying the activity in ULIRGs, regardless of the powering source in their nuclei. Also common to Arp 220 and Mrk 231 is the outstanding $H^{13}CN/C^{18}O$ ratio, as previously commented in Sect. 6. Again, if $C^{18}O$ is overabundant in Arp 220 and Mrk 231, it only makes the difference in abundances of HC_3N and $H^{13}CN$ between the ULIRGs and the rest of the sample even clearer. On the other hand, if $C^{18}O$ has similar values in all the galaxies, it results in an even stronger contrast.

It is also interesting to compare ULIRGs, which are characterised by strong interactions between galaxies, with isolated galaxies, where the chemical and physical properties are the result of intrinsic and secular mechanisms. In CIG 638, a good representative of an isolated galaxy (see Verley et al. 2007 for the criteria used to define these objects), the C_2H/HCN and C_2H/HNC integrated intensity ratios were found to be interestingly high (1.0 and 4.3, respectively), either because the galaxy has a lower amount of dense gas, or/and due to an overproduction of C_2H (Martín et al. 2014). The C_2H/HCN ratios for Arp 220 and Mrk 231 are a factor of 3 and 4 (respectively) lower than in CIG 638. Moreover, the C_2H/HNC integrated intensity ratio is even more contrasted, being nine and five times (respectively) lower in the ULIRGs than in the isolated galaxy. This points to a very likely difference in the gas composition between these two types of galaxies, with the ULIRGs containing more dense gas (associated with their nuclear starbursts), than the isolated galaxies. On the other hand, the rest of the galaxies of our sample have a C_2H/HNC ratio in the range ~[0.7−1.5] which, according to the results derived by Martín et al. (2014), agrees with the expected values for "normal" (local) starbursts and AGNs. These results are on average well below the CIG 638 and above the values of Arp 220 and Mrk 231.

8. Summary and conclusions

Using the IRAM 30 m telescope, we performed a molecular line survey towards the circumnuclear regions of eight active galaxies, covering the frequency range ~[86−116] GHz. The sample is composed of three starburst galaxies, M 83, M 82, and NGC 253, three AGN galaxies with starburst influence, NGC 1068, M 51, and NGC 7469, and two ULIRGs, Mrk 231 and Arp 220. The column densities of 37 species (or their upper limits when they are not detected) were calculated assuming LTE and a single source size for each galaxy based on previous available interferometric maps. The studied species include ten ^{13}C, ^{18}O, ^{17}O, and ^{34}S bearing isotopologues. We compared the abundances, with respect to $C^{18}O$, of the eight galaxies to characterise the average molecular gas composition of each kind of galaxies. Our results are summarised in Figs. 1 and 6 and in Tables 2–4.

The comparison among the galaxies allowed us to find out the key species that show the most highly contrasted abundances, relative to $C^{18}O$, among the sources. CH_3CCH is only detected in starbursts and is a factor of one order of magnitude more abundant in M 82 (the galaxy with the highest abundance) than in NGC 1068 (not detected). This molecule seems to be associated with massive star formation and might be a good tracer of PDRs. $H^{13}CN$, CH_3CN and SiO have a peak of abundance in Arp 220, which is 21 ($H^{13}CN$), and 7 (CH_3CN, SiO) times higher than in M 82 (minimum abundance). We find high C_2H abundances in M 82, NGC 1068 and NGC 7469; they are five times higher in NGC 7469 than in M 51 (minimum). A large part of the C_2H emission in the AGNs is expected to come from the starburst rings that surround the CNDs. HNCO shows abundance variations among the starburst galaxies of a factor of four. This latter result supports previous claims of HNCO as a good tracer of the starburst evolutionary state (Martín et al. 2009a). Other species such as HCN and HC_3N show smaller, but still significant abundance differences among galaxies by factors of three to four. All the cited molecules constitute good candidates for studying the chemistry in galaxy nuclei.

Regarding the starburst galaxies, the molecular gas of M 83 is characterised by relatively high abundances (with respect to $C^{18}O$, 10^{-2}–10^{-4}) of some shock tracers, such as CH_3OH, HNCO and SiO, as well as the absence of both Hα recombination lines and the PDR tracers c-C_3H_2 and HCO. In NGC 253 shocks created by molecular cloud collisions and stellar winds dominate the heating of the gas, as shown by the presence of several other shock- and dust grain-tracers (e.g. SO, SO_2, OCS, $HOCO^+$). In addition, the molecular cloud complexes are ionised by OB clusters, which translates into high intensities of Hα recombination lines, as well as moderate abundances of c-C_3H_2, HOC^+, and HCO (10^{-3}–10^{-4}). Lastly, M 82 represents a galaxy where UV fields are very intense and create extended PDRs. Hα recombination lines, as well as c-C_3H_2, HCO, HOC^+ and CH_3CCH are brighter than in the other starbursts of the sample. CH_3OH and HNCO are still observable in the cores of the molecular clouds, although their abundances are clearly lower than in NGC 253 and M 83, which is due to the lack of shielding from UV photons. We explored a possible scenario where M 83, NGC 253 and M 82 are considered templates of galaxies in young, intermediate, and late phases of starbursts, and followed the evolution of the gas composition with time.

As for the AGNs (NGC 1068, NGC 7469, M 51 and Mrk 231), HCN/HCO^+ and HCN/CS are quite low in NGC 7469, similar to the values in starburst galaxies; HCN/$C^{18}O$ and CN/$C^{18}O$, C_2H/$C^{18}O$, and HNC/$C^{18}O$ are also much the same in starbursts and in the low-luminosity AGN of M 51. The lack of molecular trends in our AGN galaxies, as compared to the starbursts, seems to be due to their CNDs not being spatially resolved by the IRAM 30 m beam. Remarkably, CH_3OH, SiO and HNCO are only detected in NGC 1068.

Finally, the ULIRGs Mrk 231 and Arp 220 show common spectral features, such as the almost identical ^{13}CO and $C^{18}O$ column densities, and higher $H^{13}CN$/$C^{18}O$ and HC_3N/$C^{18}O$ abundance ratios than the rest of the galaxies. Nevertheless, both ULIRGs differ in some line detections that seem to indicate that different mechanisms are at work in their nuclear regions. In particular, Arp 220 shows emission of HC_3N vibrationally excited lines that arise from warm gas (T_{vib} = 190 ± 20 K), and shock tracers such as CH_3OH, HNCO, and SiO. This, together with the lack of PDR tracers such as HOC^+, HCO, and c-C_3H_2, makes Arp 220 resemble the spectrum of a giant hot core-like starburst. On the other hand, Mrk 231 has higher abundances of HCN, $H^{13}CN$, and HCO^+, like the values of NGC 1068 and NGC 7469, which makes it more similar to an AGN-dominated galaxy.

Acknowledgements. This work has been partially funded by MICINN grants AYA2010-21697-C05-01 and FIS2012-39162-C06-01, and Astro-Madrid (CAM S2009/ESP-1496). We wish to thank Jacques Le Bourlot and the Paris' Master of Astrophysics students for sharing their M 82 data with us, which were observed with the IRAM 30 m telescope at 3 mm wavelengths. These data were added to our own observations.

References

Aalto, S. 2008, Ap&SS, 313, 273
Aalto, S., Polatidis, A. G., Hüttemeister, S., & Curran, S. J. 2002, A&A, 381, 783
Aalto, S., Spaans, M., Wiedner, M. C., Hüttemeister, S. 2007, A&A, 464, 193
Aalto, S., García-Burillo, S., Muller, S., et al. 2012, A&A, 537, A44
Aladro, R., Martín-Pintado, J., Martín, S., Mauersberger, R., & Bayet, E. 2011a, A&A, 525, A89
Aladro, R., Martín, S., Martín-Pintado, J., et al. 2011b, A&A, 535, A84
Aladro, R., Viti, S., Bayet, E., et al. 2013, A&A, 549, A39
Anantharamaiah, K. R., Viallefond, F., Mohan, N. R., Goss, W. M., & Zhao, J. H. 2000, ApJ, 537, 613
Armijos-Abendaño, J., Martín-Pintado, J., Requena-Torres, M. A., Martín, S., & Rodríguez-Franco, A. 2015, MNRAS, 446, 3842
Bastian, N., Gieles, M., Lamers, H. J. G. L. M., Scheepmaker, R. A., & de Grijs, R. 2005, A&A, 431, 905

Bennett, C. J., Jamieson, C. S., Osamura, Y., & Kaiser, R. I. 2005, ApJ, 624, 1097
Binney, J., Gerhard, O. E., Stark, A. A., Bally, J., & Uchida, K. I. 1991, MNRAS, 252, 210
Boksenberg, A., Carswell, R. F., Allen, D. A., et al. 1977, MNRAS, 178, 451
Bolatto, A. D., Warren, S. R., Leroy, A. K., et al. 2013, Nature, 499, 450
Bradford, C. M., Nikola, T., Stacey, G. J., et al. 2003, ApJ, 586, 891
Carter, M., Lazareff, B., Maier, D., et al. 2012, A&A, 538, A89
Chengalur, J. N., & Kanekar, N. 2003, A&A, 403, L43
Chiang, Y.-K., & Kong, A. K. H. 2011, MNRAS, 414, 1329
Chin, Y.-N., Henkel, C., Whiteoak, J. B., Langer, N., & Churchwell, E. B. 1996, A&A, 305, 960
Churchwell, E., & Hollis, J. M. 1983, ApJ, 272, 591
Costagliola, F., & Aalto, S. 2010, A&A, 515, A71
Costagliola, F., Aalto, S., Rodríguez, M. I., et al. 2011, A&A, 528, A30
Davies, R. I., Tacconi, L. J., & Genzel, R. 2004, ApJ, 602, 148
Davis, T. A., Heiderman, A., Evans, N. J., & Iono, D. 2013, MNRAS, 436, 570
de Vicente, P., Martín-Pintado, J., Neri, R., & Colom, P. 2000, A&A, 361, 1058
Downes, D., & Solomon, P. M. 1998, ApJ, 507, 615
Esquej, P., Alonso-Herrero, A., González-Martín, O., et al. 2014, ApJ, 780, 86
Frerking, M. A., Wilson, R. W., Linke, R. A., & Wannier, P. G. 1980, ApJ, 240, 65
Fuente, A., García-Burillo, S., Gerin, M., et al. 2005, ApJ, 619, L155
Fuente, A., García-Burillo, S., Usero, A., et al. 2008, A&A, 492, 675
Gallagher, S. C., Brandt, W. N., Chartas, G., Garmire, G. P., & Sambruna, R. M. 2002, ApJ, 569, 655
García-Burillo, S., Martín-Pintado, J., Fuente, A., & Neri, R. 2000, A&A, 355, 499
García-Burillo, S., Martín-Pintado, J., Fuente, A., & Neri, R. 2001, ApJ, 563, L27
García-Burillo, S., Martín-Pintado, J., Fuente, A., Usero, A., & Neri, R. 2002, ApJ, 575, L55
García-Burillo, S., Usero, A., Fuente, A., et al. 2010, A&A, 519, A2
García-Burillo, S., Combes, F., Usero, A., et al. 2014, A&A, 567, A125
Genzel, R., Weitzel, L., Tacconi-Garman, L. E., et al. 1995, ApJ, 444, 129
González-Alfonso, E., Fischer, J., Graciá-Carpio, J., et al. 2014, A&A, 561, A27
Greve, T. R., Papadopoulos, P. P., Gao, Y., & Radford, S. J. E. 2009, ApJ, 692, 1432
Guzmán, V. V., Pety, J., Gratier, P., et al. 2014, FaDi, 168, 103
Helfer, T. T., & Blitz, L. 1995, ApJ, 450, 90
Henkel, C., Asiri, H., Ao, Y., et al. 2014, A&A, 565, A3
Hollis, J. M., & Churchwell, E. 1983, ApJ, 271, 170
Houghton, R. C. W., & Thatte, N. 2008, MNRAS, 385, 1110
Huettemeister, S., Henkel, C., Mauersberger, R., et al. 1995, A&A, 295, 571
Irvine, W. M., Hoglund, B., Friberg, P., Askne, J., & Ellder, J. 1981, ApJ, 248, L113
Izumi, T., Kohno, K., Martín, S., et al. 2013, PASJ, 65, 100
Jiménez-Serra, I., Caselli, P., Martín-Pintado, J., & Hartquist, T. W. 2008, A&A, 482, 549
Knudsen, K. K., Walter, F., Weiss, A., et al. 2007, ApJ, 666, 156
Kohno, K., Kawabe, R., Tosaki, T., & Okumura, S. K. 1996, ApJ, 461, L29
Kohno, K., Matsushita, S., Vila-Vilaró, B., et al. 2001, The Central Kiloparsec of Starbursts and AGN: The La Palma Connection, 249, 672
Krips, M., Neri, R., García-Burillo, S., et al. 2008, ApJ, 677, 262
Krips, M., Martín, S., Eckart, A., et al. 2011, ApJ, 736, 37
Lepp, S., & Dalgarno, A. 1996, A&A, 306, L21
Lindberg, J. E., Aalto, S., Costagliola, F., et al. 2011, A&A, 527, A150
Markwick, A. J., Charnley, S. B., Butner, H. M., & Millar, T. J. 2005, ApJ, 627, L117
Martín-Pintado, J., Bachiller, R., & Fuente, A. 1992, A&A, 254, 315
Martín-Pintado, J., de Vicente, P., Fuente, A., & Planesas, P. 1997, ApJ, 482, L45
Martín-Pintado, J., de Vicente, P., Rodríguez-Fernández, N. J., Fuente, A., & Planesas, P. 2000, A&A, 356, L5
Martín-Pintado, J., Jiménez-Serra, I., Rodríguez-Franco, A., Martín, S., & Thum, C. 2005, ApJ, 628, L61
Martín, S., Mauersberger, R., Martín-Pintado, J., García-Burillo, S., & Henkel, C. 2003, A&A, 411, L465
Martín, S., Martín-Pintado, J., Mauersberger, R., Henkel, C., & García-Burillo, S. 2005, ApJ, 620, 210
Martín, S., Martín-Pintado, J., & Mauersberger, R. 2006a, A&A, 450, L13
Martín, S., Mauersberger, R., Martín-Pintado, J., Henkel, C., & García-Burillo, S. 2006b, ApJS, 164, 450
Martín, S., Requena-Torres, M. A., Martín-Pintado, J., & Mauersberger, R. 2008, ApJ, 678, 245
Martín, S., Martín-Pintado, J., & Mauersberger, R. 2009a, ApJ, 694, 610
Martín, S., Martín-Pintado, J., & Viti, S. 2009b, ApJ, 706, 1323
Martín, S., Aladro, R., Martín-Pintado, J., & Mauersberger, R. 2010, A&A, 522, A62
Martín, S., Krips, M., Martín-Pintado, J., et al. 2011, A&A, 527, A36
Martín, S., Verdes-Montenegro, L., Aladro, R., et al. 2014, A&A, 563, L6
Martín, S., Kohno, K., Izumi, T., et al. 2015, A&A, 573, A116
Matsushita, S., Kohno, K., Vila-Vilaro, B., Tosaki, T., & Kawabe, R. 1998, ApJ, 495, 267
Matsushita, S., Iono, D., Petitpas, G. R., et al. 2009, ApJ, 693, 56
Meier, D. S., & Turner, J. L. 2005, ApJ, 618, 259
Meier, D. S., Walter, F., Bolatto, A. D., et al. 2015, ApJ, 801, 63
Meijerink, R., & Spaans, M. 2005, A&A, 436, 397
Meijerink, R., Spaans, M., & Israel, F. P. 2007, A&A, 461, 793
Miettinen, O., Harju, J., Haikala, L. K., & Pomrén, C. 2006, A&A, 460, 721
Müller, H. S. P., Thorwirth, S., Roth, D. A., & Winnewisser, G. 2001, A&A, 370, L49
Müller, H. S. P., Schlöder, F., Stutzki, J., & Winnewisser, G. 2005, J. Mol. Struct., 742, 215
Muller, S., Beelen, A., Guélin, M., et al. 2011, A&A, 535, A103
Muraoka, K., Kohno, K., Tosaki, T., et al. 2009, PASJ, 61, 163
Osterbrock, D. E., & Martel, A. 1993, ApJ, 414, 552
Penzias, A. A., & Burrus, C. A. 1973, ARA&A, 11, 51
Pickett, H. M., Poynter, I. R. L., Cohen, E. A., et al. 1998, J. Quant. Spect. Rad. Transf., 60, 883
Rathborne, J. M., Lada, C. J., Muench, A. A., Alves, J. F., & Lombardi, M. 2008, ApJS, 174, 396
Riquelme, D., Bronfman, L., Mauersberger, R., May, J., & Wilson, T. L. 2010, A&A, 523, A45
Sakamoto, K., Aalto, S., Wilner, D. J., et al. 2009, ApJ, 700, L104
Sakamoto, K., Mao, R.-Q., Matsushita, S., et al. 2011, ApJ, 735, 19
Sanders, D. B., Mazzarella, J. M., Kim, D.-C., Surace, J. A., & Soifer, B. T. 2003, AJ, 126, 1607
Savage, C., & Ziurys, L. M. 2004, ApJ, 616, 966
Schinnerer, E., Eckart, A., Tacconi, L. J., Genzel, R., & Downes, D. 2000, ApJ, 533, 850
Schuster, K. F., Kramer, C., Hitschfeld, M., Garcia-Burillo, S., & Mookerjea, B. 2007, A&A, 461, 143
Spaans, M., & Meijerink, R. 2007, ApJ, 664, L23
Sternberg, A., & Dalgarno, A. 1995, ApJS, 99, 565
Strickland, D. K., Heckman, T. M., Colbert, E. J. M., Hoopes, C. G., & Weaver, K. A. 2004, ApJS, 151, 193
Suzuki, H., Yamamoto, S., Ohishi, M., et al. 1992, ApJ, 392, 551
Takano, S., Nakajima, T., Kohno, K., et al. 2014, PASJ, 66, 75
Taniguchi, Y., Ohyama, Y., & Sanders, D. B. 1999, ApJ, 522, 214
Taylor, G. B., Silver, C. S., Ulvestad, J. S., & Carilli, C. L. 1999, ApJ, 519, 185
Thaddeus, P., Vrtilek, J. M., & Gottlieb, C. A. 1985, ApJ, 299, L63
Tunnard, R., Greve, T. R., Garcia-Burillo, S., et al. 2015, ApJ, 800, 25
Turner, J. L., & Ho, P. T. P. 1985, ApJ, 299, L77
Usero, A., García-Burillo, S., Fuente, A., Martín-Pintado, J., & Rodríguez-Fernández, N. J. 2004, A&A, 419, 897
van der Werf, P. P., Isaak, K. G., Meijerink, R., et al. 2010, A&A, 518, L42
Verley, S., Leon, S., Verdes-Montenegro, L., et al. 2007, A&A, 472, 121
Viti, S., Caselli, P., Hartquist, T. W., & Williams, D. A. 2001, A&A, 370, 1017
Viti, S., García-Burillo, S., Fuente, A., et al. 2014, A&A, 570, A28
Walter, F., Brinks, E., de Blok, W. J. G., et al. 2008, AJ, 136, 2563
Watanabe, Y., Sakai, N., Sorai, K., & Yamamoto, S. 2014, ApJ, 788, 4
Wilson, A. S., Helfer, T. T., Haniff, C. A., & Ward, M. J. 1991, ApJ, 381, 79

Pages 16 to 22 are available in the electronic edition of the journal at http://www.aanda.org

Appendix A: Simulated fit results for individual spectra

Table A.1. Results for M 83.

Line	Frequency MHz	I K km s^{-1}	$V_{\rm LSR}$ km s^{-1}	ΔV km s^{-1}	$T_{\rm MB}^{\rm peak}$ mK	Comments
$H^{13}CN$ (1–0)	86 340.2	0.25 ± 0.04	503.4 ± 6.8	64.7 ± 16.0	3.55	*hf*, *t*
$H^{13}CO^+$ (1–0)	86 754.3	0.21 ± 0.06	510	95	2.07	*t*
SiO (2 – 1)	86 847.0	0.24 ± 0.06	510	95	2.40	*t*
$HN^{13}C$ (1–0)	87 090.8	0.11 ± 0.05	510	95	1.11	*t*
C_2H (1–0)	87 316.9	4.01 ± 0.08	504.3 ± 1.3	91.7 ± 3.2	22.62	*hf*
HNCO ($4_{0,4}$–$3_{0,3}$)	87 925.2	0.69 ± 0.09	510	95	6.79	*m*
HCN (1–0)	88 631.8	10.18 ± 0.13	501.7 ± 0.8	95.5 ± 1.8	97.47	*hf*
HCO^+ (1–0)	89 188.6	9.30 ± 0.15	502.8 ± 1.0	95.0 ± 2.4	90.96	
HOC^+ (1–0)	89 487.4	0.29 ± 0.04	516.3 ± 7.7	95	2.87	*t*
HNC (1–0)	90 663.6	4.12 ± 0.08	505.3 ± 1.3	93.0 ± 3.0	41.45	
HC_3N (10–9)	90 979.0	0.44 ± 0.05	512.8 ± 6.4	95	4.34	
CH_3CN (5_k–4_k)	91 987.0	0.24 ± 0.06	510	95	2.33	*m*, *t*
N_2H^+ (1–0)	93 173.7	1.17 ± 0.05	510	95	13.32	*m*
$C^{34}S$ (2–1)	96 412.9	0.42 ± 0.05	510	95	4.19	
CH_3OH (2_k–1_k)	96 741.4	1.08 ± 0.05	504.1 ± 1.9	57.5 ± 4.5	17.13	m
CS (2 – 1)	97 981.0	3.25 ± 0.07	501.9 ± 1.4	95	32.04	
SO (2_1–3_2)	99 299.9	0.45 ± 0.05	503.3 ± 9.3	120.0 ± 22.1	3.49	*t*
HC_3N (11–10)	100 076.4	0.36 ± 0.04	512.8 ± 6.4	95	3.51	*t*
CH_3CCH (6_k–5_k)	102 548.0	0.44 ± 0.05	521.5 ± 22.2	95	4.23	*m*, *t*
CH_3OH (0_0–1_{-1})	108 893.9	0.20 ± 0.01	504.1 ± 1.9	57.5 ± 4.5	3.28	*t*
HC_3N (12–11)	109 173.6	0.26 ± 0.03	512.8 ± 6.4	95	2.61	*t*
$C^{18}O$ (1–0)	109 782.2	3.40 ± 0.07	502.2 ± 1.3	94.7 ± 3.1	33.65	
HNCO ($5_{0,5}$ – $4_{0,4}$)	109 905.8	0.70 ± 0.09	510	95	6.87	*m*
^{13}CO (1–0)	110 201.4	17.29 ± 0.24	502.2 ± 0.9	97.8 ± 2.1	165.00	
CH_3CN (6_k–5_k)	110 383.5	0.27 ± 0.06	510	95	2.65	*m*, *t*
$C^{17}O$ (1–0)	112 359.3	0.63 ± 0.06	510	95	6.24	*t*
CN ($1_{0,1}$–$0_{0,1}$)	113 191.3	6.31 ± 0.06	500.7 ± 0.9	118.4 ± 2.2	31.14	*m*
CN ($1_{0,2}$–$0_{0,1}$)	113 491.0	12.66 ± 0.13	500.7 ± 0.9	118.4 ± 2.2	91.81	*m*
^{12}CO (1–0)	115 271.2	225.92 ± 2.85	504.4 ± 1.3	79.6 ± 2.8	1940.18	

Notes. Remarks: (*b*) blended line; (*m*) multi-transition line; (*hf*) hyperfine transition; (*t*) tentative detection. Parameters without errors were fixed when fitting the lines.

Table A.2. Results for NGC 253.

Line	Frequency MHz	I K km s^{-1}	$V_{\rm LSR}$ km s^{-1}	ΔV km s^{-1}	$T_{\rm MB}^{\rm peak}$ mK	Comments
NH_2CN ($4_{1,3}-3_{1,2}$)	80 504.6	0.70 ± 0.15	250	180	3.68	*t*
C_2S (6_7-5_6)	81 505.2	0.66 ± 0.18	250	200	3.08	*t*
HC_3N (9−8)	81 881.5	7.37 ± 0.15	250	180	38.41	
c-C_3H_2 ($2_{0,2}-1_{1,1}$)	82 093.6	1.66 ± 0.07	250	180	8.67	
HC_5N (31−30)	82 539.3	0.99 ± 0.45	240	180	5.15	*t*
c-C_3H_2 ($3_{1,2}-3_{0,3}$)	82 966.2	0.76 ± 0.03	250	180	3.94	*t*
CH_3OH ($5_{-1}-4_0$)	84 521.2	2.52 ± 0.12	249.4 ± 5.1	217.7 ± 11.9	10.9	
OCS (7 − 6)	85 139.1	1.39 ± 0.08	250	200	6.53	*b*
$HC^{18}O^+$ (1−2)	85 162.2	0.84 ± 0.04	250	200	3.93	*b*
HC_5N (32-31)	85 201.6	0.92 ± 0.41	240	180	4.78	*b*
c-C_3H_2 ($2_{1,2}-1_{0,1}$)	85 338.9	5.99 ± 0.26	250	180	31.09	
CH_3CCH (5_K-4_K)	85 457.3	2.66 ± 0.29	250	200	12.39	*m*
$HOCO^+$ ($4_{0,4}-3_{0,3}$)	85 531.5	0.38 ± 0.22	250	180	1.98	*t*
H42α	85 688.4	–	230	180	8	*b*
SO (2_2-1_1)	86 094.0	0.88 ± 0.07	250	180	4.60	
$H^{13}CN$ (1−0)	86 340.2	4.71 ± 0.13	250.1 ± 3.2	181.5 ± 7.4	24.25	*hf*
HCO ($1_{1,0}-0_{1,0}$)	86 670.8	1.92 ± 1.17	250	200	4.68	*b*, *hf*
$H^{13}CO^+$ (1−0)	86 754.3	3.81 ± 0.44	250	200	17.86	*b*
SiO (2 − 1)	86 847.0	4.76 ± 0.44	250	200	22.30	
$HN^{13}C$ (1−0)	87 090.8	2.09 ± 0.12	250	200	9.81	
C_2H (1−0)	87 316.9	34.64 ± 0.45	246.9 ± 1.9	186.8 ± 3.8	106.10	*hf*
HC_5N (33−32)	87 863.9	0.84 ± 0.38	240	180	4.39	*t*, *b*
HNCO ($4_{0,4}-3_{0,3}$)	87 925.2	5.79 ± 1.73	250	200	26.99	*m*, *b*
HCN (1−0)	88 631.8	68.37 ± 0.72	249.1 ± 1.3	199.7 ± 3.1	305.20	*hf*
HCO^+ (1−0)	89 188.6	57.92 ± 0.63	254.8 ± 1.4	199.7 ± 3.4	266.77	
HOC^+(1−0)	89 487.4	2.13 ± 0.11	250	200	10.02	
HNC (1−0)	90 663.6	35.45 ± 0.27	238.6 ± 0.9	185.1 ± 2.2	177.46	*b*
HC_5N (34−33)	90 526.2	0.76 ± 0.34	240	180	3.99	*t*, *b*
HC_3N (10−9)	90 979.0	8.42 ± 0.18	250	180	43.90	
CH_3CN (5_k-4_k)	91 987.0	3.59 ± 2.66	250	180	18.55	*m*, *b*
H41α	92 034.4	–	230	180	5	*b*
^{13}CS (2−1)	92 494.3	0.99 ± 0.07	250	200	4.65	
N_2H^+ (1−0)	93 173.7	10.64 ± 0.19	235.7 ± 2.0	180	54.89	*m*, *b*
HC_5N (35−34)	93 188.5	0.69 ± 0.31	240	180	3.59	*t*, *b*
CH_3CHO ($5_{1,5}-4_{1,4}$) A	93 580.9	0.52 ± 4.05	250	200	2.44	*t*
CH_3CHO ($5_{1,5}-4_{1,4}$) E	93 595.2	0.52 ± 4.03	250	200	2.43	*t*
C_2S (7_8-6_7)	93 870.1	0.68 ± 0.19	250	200	3.18	*t*
CH_3OH (8_0-7_1)	95 169.4	0.98 ± 0.12	233.3 ± 10.6	171.8 ± 24.2	5.38	
HC_5N (36−35)	95 850.7	0.61 ± 0.28	240	180	3.21	*t*, *b*
CH_3OH (2_1-1_1)	95 914.3	0.81 ± 0.01	250	200	3.80	*b*
CH_3CHO ($5_{0,5}-4_{0,4}$) E	95 947.4	0.65 ± 5.03	250	200	3.04	*b*, *t*
CH_3CHO ($5_{0,5}-4_{0,4}$) A	95 963.4	0.65 ± 5.06	250	200	3.06	*b*, *t*
$C^{34}S$ (2−1)	96 412.9	4.39 ± 0.13	250	200	20.58	
CH_3OH (2_k-1_k)	96 741.4	17.14 ± 0.26	250	200	78.40	*m*, *b*
OCS (8−7)	97 301.2	1.38 ± 0.08	250	200	6.47	
CH_3OH (2_1-1_1)	97 582.8	0.83 ± 0.01	250	200	3.89	
CS (2−1)	97 981.0	33.98 ± 0.46	234.5 ± 1.7	195.2 ± 4.1	162	
HC_5N (37−36)	98 512.9	0.54 ± 0.24	240	180	2.83	*t*
H40α	99 023.0	1.45 ± 0.50	237	180	7	
SO (2_3-1_2)	99 299.9	4.20 ± 0.32	250	180	21.91	*b*
NH_2CN ($5_{1,5}-4_{1,4}$)	99 311.2	1.07 ± 0.23	250	180	5.58	*m*, *b*
NH_2CN ($5_{0,5}-4_{0,4}$)	99 972.7	1.06 ± 0.23	250	180	5.51	
HC_3N (11−10)	100 076.4	9.02 ± 0.19	250	180	47.02	
NH_2CN ($5_{1,4}-4_{1,3}$)	100 629.5	1.09 ± 0.24	250	180	5.66	*m*
HC_5N (38−37)	101 175.1	0.48 ± 0.21	240	180	2.49	*t*
H_2CS ($3_{1,3}-2_{1,2}$)	101 477.6	0.58 ± 0.12	250	180	3.02	*t*
CH_3CCH (6_k-5_k)	102 548.0	3.89 ± 0.42	250	200	18.10	*m*
H_2CS ($3_{0,3}-2_{0,2}$)	103 040.2	0.83 ± 0.18	250	180	4.33	*t*
HC_5N (39−38)	103 837.3	0.41 ± 0.19	240	180	2.16	*t*
SO_2 ($3_{1,3}-2_{0,2}$)	104 029.4	0.56 ± 0.32	240	180	2.90	*t*
H_2CS ($3_{1,2}-2_{1,1}$)	104 617.0	0.60 ± 0.13	250	180	3.15	*t*
C_2S (8_9-7_8)	106 349.7	0.61 ± 0.17	250	200	2.87	*t*
H39α	106 737.4	1.75 ± 0.34	220	181	9	

Notes. See caption of Table A.1 for details.

Table A.2. continued.

Line	Frequency MHz	I K km s^{-1}	$V_{\rm LSR}$ km s^{-1}	ΔV km s^{-1}	$T_{\rm MB}^{\rm peak}$ mK	Comments
$HOCO^+$ ($5_{0,5}$–$4_{0,4}$)	106 913.6	0.59 ± 0.34	250	180	3.07	*t*
^{13}CN ($1_{2,1}$–$0_{1,0}$)	108 651.3	1.08 ± 0.09	250	200	9.72	*m*, *b*
^{13}CN ($1_{1,1}$–$0_{1,1}$)	108 657.6	1.08 ± 0.09	250	200	9.72	*m*, *b*
^{13}CN ($1_{2,2}$–$0_{1,1}$)	108 780.2	1.94 ± 0.16	250	200	8.92	*m*
CH_3OH (0_0–1_{-1})	108 893.9	3.50 ± 0.05	250	200	16.39	
HC_3N (12–11)	109 173.6	9.12 ± 0.19	250	180	47.56	
SO (3_2–2_1)	109 252.2	1.40 ± 0.11	250	180	7.28	*t*
OCS (9–8)	109 463.1	1.20 ± 0.07	250	200	5.65	*b*, *t*
$C^{18}O$ (1–0)	109 782.2	22.49 ± 0.57	258.3 ± 3.3	204.5 ± 7.8	102.65	
HNCO ($5_{0,5}$–$4_{0,4}$)	109 905.8	7.62 ± 2.28	250	200	35.55	*m*
^{13}CO (1–0)	110 201.4	81.16 ± 0.96	259.9 ± 1.6	200.8 ± 3.6	370.67	
CH_3CN (6_k–5_k)	110 383.5	5.03 ± 3.73	250	180	25.94	*m*
$C^{17}O$ (1–0)	112 359.3	3.15 ± 0.14	269.9 ± 5.7	200	14.77	
CN ($1_{0,1}$–$0_{0,1}$)	113 191.3	47.93 ± 0.32	249.6 ± 0.8	193.2 ± 2.0	184.30	*m*
CN ($1_{0,2}$–$0_{0,1}$)	113 491.0	95.53 ± 0.62	249.6 ± 0.8	193.2 ± 2.0	425.50	*m*
NS ($3_{1,-1}$–$2_{1,1}$)	115 153.9	1.80 ± 0.90	250	180	8.86	*m*, *b*, *t*
^{12}CO (1–0)	115 271.2	1069.30 ± 8.60	260.9 ± 0.1	210.6 ± 0.1	4769.30	*b*
H38α	115 274.4	–	230	180	7	b
NS ($3_{1,1}$–$2_{1,-1}$)	115 556.2	1.80 ± 0.90	250	180	8.32	*m*, *t*

Table A.3. Results for M 82.

Line	Frequency MHz	I K km s^{-1}	$V_{\rm LSR}$ km s^{-1}	ΔV km s^{-1}	$T_{\rm MB}^{\rm peak}$ mK	Comments
c-C_3H_2 ($3_{2,2}$–$3_{1,3}$)	84 727.7	0.143 ± 0.06	300	100	1.34	*t*
$HC^{18}O^+$ (1–0)	85 162.2	0.41 ± 0.06	300	100	3.82	*b*
c-C_3H_2 ($2_{1,2}$–$1_{1,0}$)	85 338.9	3.36 ± 0.13	300	100	31.16	
CH_3CCH (5_k–4_k)	85 457.3	2.59 ± 0.08	314.6 ± 1.9	100	23.94	*m*
H42α	85 688.4	–	310	100	11	*b*
$H^{13}CN$ (1–0)	86 340.2	0.38 ± 0.04	300	100	3.54	*hf*, *t*
HCO ($1_{1,0}$–$0_{1,0}$)	86 670.8	0.32 ± 0.03	300	100	2.99	*b*, *t*
$H^{13}CO^+$ (1–0)	86 754.3	0.89 ± 0.04	300	100	8.39	*b*
SiO (2–1)	86 847.0	0.30 ± 0.04	300	100	2.87	*b*, *t*
C_2H (1–0)	87 316.9	20.61 ± 0.23	294.1 ± 1.1	134.2 ± 2.4	83.31	*hf*
HNCO ($4_{0,4}$–$3_{0,3}$)	87 925.2	0.26 ± 0.45	300	100	2.41	*m*, *t*
HCN (1–0)	88 631.8	23.56 ± 0.40	294.1 ± 1.1	113.6 ± 2.6	182.00	*hf*
HCO^+ (1–0)	89 188.6	33.74 ± 0.80	292.8 ± 1.6	128.8 ± 3.7	236	
HOC^+ (1–0)	89 487.4	0.56 ± 0.04	300	100	5.21	
HNC(1–0)	90 663.6	10.48 ± 0.23	296.3 ± 1.6	115.8 ± 3.8	83.79	
HC_3N (10–9)	90 979.0	1.42 ± 0.03	305.7 ± 1.5	109.5 ± 3.4	11.64	
CH_3CN (5_k–4_k)	91 987.0	0.24 ± 0.72	300	100	2.19	*m*, *b*
H41α	92 034.4	–	280	120	9	*b*
N_2H^+ (1–0)	93 173.7	1.65 ± 0.04	299.5 ± 1.5	100	15.35	*m*
CH_3CHO ($5_{1,5}$–$4_{1,4}$) A	93 580.9	0.26 ± 0.02	300	100	2.12	m, *t*
$C^{34}S$ (2–1)	96 412.9	0.58 ± 0.03	294.9 ± 3.3	100	5.46	
CH_3OH (2_k–1_k)	96 741.4	1.01 ± 0.03	300	100	9.17	*m*
CS (2–1)	97 981.0	9.97 ± 0.16	294.8 ± 1.1	109.2 ± 2.6	84.66	
H40α	99 023.0	1.40 ± 0.70	302 ± 8	100	13	
SO (2_1–3_2)	99 299.9	1.11 ± 0.11	300	100	10.39	
HC_3N (11–10)	100 076.4	1.42 ± 0.03	305.7 ± 1.5	109.5 ± 3.4	12.26	
CH_3CCH (6_k–5_k)	102 548.0	3.48 ± 0.11	314.6 ± 1.9	100	32.01	*m*
H39α	106 737.4	1.00 ± 0.50	307.2 ± 5.4	100	9	
CH_3OH (0_0–1_{-1})	108 893.9	0.254 ± 0.009	300	100	2.39	m
HC_3N (12–11)	109 173.6	1.34 ± 0.03	305.7 ± 1.5	109.5 ± 3.4	12.14	
$C^{18}O$ (1–0)	109 782.2	5.78 ± 0.10	300.4 ± 1.5	103.0 ± 3.5	52.35	
HNCO ($5_{0,5}$–$4_{0,4}$)	109 905.8	0.45 ± 0.79	300	100	4.23	*m*, *t*
^{13}CO (1–0)	110 201.4	28.25 ± 0.39	297.3 ± 1.0	107.1 ± 2.3	240.09	
CH_3CN (6_k–5_k)	110 383.5	0.28 ± 0.85	300	100	2.56	m, t
$C^{17}O$ (1–0)	112 359.3	0.38 ± 0.07	300	100	3.55	t
CN ($1_{0,1}$–$0_{0,1}$)	113 191.3	14.34 ± 0.19	291.5 ± 1.1	122.2 ± 2.8	69.10	*m*
CN ($1_{0,2}$–$0_{0,1}$)	113 491.0	28.63 ± 0.37	291.5 ± 1.1	122.2 ± 2.8	194.80	*m*
NS ($3_{1,-1}$–$2_{1,1}$)	115 153.9	0.73 ± 0.13	300	100	6.11	*m*, *b*, *t*
^{12}CO (1–0)	115 271.2	535.8 ± 2.85	294.3 ± 1.4	94.4 ± 3.1	3892.23	*b*
Hα38	115 274.4	–	300	100	9	*b*
NS ($3_{1,1}$–$2_{1,-1}$)	115 556.2	0.73 ± 0.13	300	100	5.55	*m*, *t*

Notes. See caption of Table A.1 for details.

Table A.4. Results for M 51.

Line	Frequency MHz	I K km s^{-1}	$V_{\rm LSR}$ km s^{-1}	ΔV km s^{-1}	$T_{\rm MB}^{\rm peak}$ mK	Comments
$H^{13}CN$ (1–0)	86 340.2	0.19 ± 0.04	470	130	1.38	*hf*, *t*
C_2H (1–0)	87 316.9	1.26 ± 0.07	466.6 ± 5.5	140.4 ± 12.2	5.04	*hf*
HCN (1–0)	88 631.8	5.39 ± 0.10	473.0 ± 1.5	129.1 ± 3.6	38.75	*hf*
HCO^+ (1–0)	89 188.6	2.67 ± 0.07	473.3 ± 2.2	132.0 ± 5.1	18.98	
HNC (1–0)	90 663.6	1.79 ± 0.06	472.9 ± 2.6	126.7 ± 6.0	13.23	
N_2H^+ (1–0)	93 173.7	0.74 ± 0.04	466.4 ± 5.5	146.8 ± 13.0	4.70	*m*
$C^{34}S$ (2–1)	96 412.9	0.17 ± 0.04	470	130	1.24	*t*
CH_3OH (2_k–1_k)	96 741.4	0.24 ± 0.06	470	130	1.72	*m*, *t*
CS (2–1)	97 981.0	1.04 ± 0.05	464.8 ± 4.1	125.6 ± 9.6	7.74	
SO (2_1–3_2)	99 299.9	0.25 ± 0.06	470	130	1.80	*t*
$C^{18}O$ (1–0)	109 782.2	1.61 ± 0.09	474.3 ± 4.7	133.5 ± 11.1	11.34	
^{13}CO (1–0)	110 201.4	6.68 ± 0.25	469.7 ± 3.0	123.9 ± 7.1	50.40	
$C^{17}O$ (1–0)	112 359.3	0.30 ± 0.06	470	130	2.14	*t*
CN ($1_{0,1}$–$0_{0,1}$)	113 191.3	2.55 ± 0.04	468.4 ± 1.3	130.0 ± 3.4	12.16	*m*
CN ($1_{0,2}$–$0_{0,1}$)	113 491.0	5.12 ± 0.07	468.4 ± 1.3	130.0 ± 3.4	34.53	*m*
^{12}CO (1–0)	115 271.2	50.14 ± 1.53	468.5 ± 2.5	120.0 ± 5.7	379.30	

Notes. See caption of Table A.1 for details.

Table A.5. Results for NGC 1068.

Line	Frequency MHz	I K km s^{-1}	$V_{\rm LSR}$ km s^{-1}	ΔV km s^{-1}	$T_{\rm MB}^{\rm peak}$ mK	Comments
$H^{13}CN$ (1–0)	86 340.2	0.78 ± 0.08	1088.4 ± 11.2	180	4.03	*hf*
HCO ($1_{1,0}$–$0_{1,0}$)	86 670.8	0.49 ± 0.12	1100	240	1.08	*t*, *b*, *hf*
SiO (2–1)	86 847.0	0.60 ± 0.07	1100	240	2.36	*t*
$HN^{13}C$ (1–0)	87 090.8	0.19 ± 0.05	1100	150	1.20	*t*
C_2H (1–0)	87 316.9	7.80 ± 0.10	1106.4 ± 2.6	239.8 ± 5.3	18.51	*b*, *hf*
HNCO ($4_{0,4}$–$3_{0,3}$)	87 925.2	0.57 ± 0.89	1100	240	2.20	*m*, *t*, *b*
HCN (1–0)	88 631.8	23.55 ± 0.28	1112.8 ± 1.6	215.9 ± 3.4	77.84	*hf*
HCO^+ (1–0)	89 188.6	14.36 ± 0.17	1113.7 ± 1.9	219.3 ± 4.2	56.30	
HOC^+(1–0)	89 487.4	0.31 ± 0.06	1110	234.1 ± 73.4	1.23	*t*
HNC(1–0)	90 663.6	7.78 ± 0.10	1112.2 ± 1.9	225.1 ± 4.4	31.12	
HC_3N (10–9)	90 979.0	0.71 ± 0.03	1091.0 ± 5.6	190	3.52	
CH_3CN (5_k–4_k)	91 987.0	0.59 ± 0.42	1100	240	2.30	*m*, *t*
N_2H^+ (1–0)	93 173.7	1.99 ± 0.08	1100.6 ± 5.4	240	7.62	m
$C^{34}S$ (2–1)	96 412.9	0.68 ± 0.08	1100	240	2.64	*t*
CH_3OH (2_k–1_k)	96 741.4	1.55 ± 0.09	1100	240	5.93	*m*
CS (2–1)	97 981.0	3.95 ± 0.09	1092.8 ± 3.3	212.2 ± 7.6	17.14	*b*
SO (2_1–3_2)	99 299.9	0.47 ± 0.06	1065.1 ± 12.4	139.7 ± 29.0	3.13	
HC_3N (11–10)	100 076.4	0.80 ± 0.04	1091.0 ± 5.6	190	3.95	
HC_3N (12–11)	109 173.6	0.85 ± 0.04	1091.0 ± 5.6	190	4.19	*t*
$C^{18}O$ (1–0)	109 782.2	3.90 ± 0.09	1100.5 ± 4.0	258.0 ± 9.4	14.02	
^{13}CO (1–0)	110 201.4	13.10 ± 0.24	1100.8 ± 2.9	237.6 ± 5.8	49.36	
CH_3CN (6_k–5_k)	110 383.5	0.70 ± 0.49	1100	240	2.71	*m*, *t*
CN ($1_{0,1}$–$0_{0,1}$)	113 191.3	13.15 ± 0.10	1114.0 ± 1.0	224.4 ± 2.5	43.20	*m*
CN ($1_{0,2}$–$0_{0,1}$)	113 491.0	25.79 ± 0.19	1110.4 ± 1.0	224.4 ± 2.5	87.19	*m*
^{12}CO (1–0)	115 271.2	81.30 ± 1.01	1168.1 ± 10.2	122.5 ± 10.8	624.39	*m*

Notes. CO was fitted with a triple Gaussian, and its parameters refer to the central one. See caption of Table A.1 for more details.

Table A.6. Results for NGC 7469.

Line	Frequency MHz	I K km s^{-1}	$V_{\rm LSR}$ km s^{-1}	ΔV km s^{-1}	$T_{\rm MB}^{\rm peak}$ mK	Comments
C_2H (1−0)	87 316.9	1.58 ± 0.14	4894.1 ± 17.8	233.0 ± 35.1	4.19	*hf*
HCN (1−0)	88 631.8	2.36 ± 0.13	4854.3 ± 8.7	239.2 ± 20.4	9.18	*hf*
HCO^+ (1−0)	89 188.6	2.89 ± 0.14	4847.3 ± 8.0	247.5 ± 18.7	10.90	
HNC (1−0)	90 663.6	1.08 ± 0.12	4852.1 ± 18.3	250	4.07	
CS (2−1)	97 981.0	0.93 ± 0.09	4871.0 ± 15.3	251.2 ± 36.0	3.48	*t*
$C^{18}O$ (1−0)	109 782.2	0.42 ± 0.08	4850	250	1.58	*t*
^{13}CO (1−0)	110 201.4	2.34 ± 0.10	4849.5 ± 6.9	245.9 ± 16.1	8.92	
CN ($1_{0,1}$−$0_{0,1}$)	113 191.3	1.92 ± 0.07	4847.3 ± 5.9	248.0 ± 14.4	6.33	*m*, *t*
CN ($1_{0,2}$−$0_{0,1}$)	113 491.0	3.85 ± 0.49	4847.3 ± 5.9	248.0 ± 14.4	14.14	*m*
^{12}CO (1−0)	115 271.2	58.12 ± 1.51	4847.0 ± 7.6	236.6 ± 10.1	208.61	

Notes. See caption of Table A.1 for details.

Table A.7. Results for Arp 220.

Line	Frequency MHz	I K km s^{-1}	$V_{\rm LSR}$ km s^{-1}	ΔV km s^{-1}	$T_{\rm MB}^{\rm peak}$ mK	Comments
$H^{13}CN$ (1−0)	86 340.2	1.65 ± 0.09	5364.1 ± 11.1	328.0 ± 25.6	4.46	*hf*
$H^{13}CO^+$ (1−0)	86 754.3	0.40 ± 0.34	5350	390	0.95	*b*, *t*
SiO (2−1)	86 847.0	1.35 ± 0.18	5350	363.8 ± 44.0	3.42	*b*
C_2H (1−0)	87 316.9	3.84 ± 0.13	5317.3 ± 11.5	388.2 ± 32.5	6.29	*hf*
HCN (1−0)	88 631.8	11.06 ± 0.24	5339.1 ± 6.1	448.1 ± 13.2	18.02	*hf*
HCO^+ (1−0)	89 188.6	4.62 ± 0.21	5312.8 ± 14.3	450	9.13	
HNC(1−0)	90 663.6	7.78 ± 0.34	5326.7 ± 12.7	378.8 ± 27.8	17.24	
HC_3N (10−9)	90 979.0	3.38 ± 0.09	5331.4 ± 7.4	386.7 ± 17.4	8.11	
HC_3N, $v7 = 1$ (10_{-1}−9_1)	91 202.7	0.39 ± 1.01	5331	390	1.67	*t*
HC_3N, $v7 = 1$ (10_1−9_{-1})	91 333.4	0.69 ± 1.01	5331	390	1.67	*t*
CH_3CN (5_k−4_k)	91 987.0	1.41 ± 0.20	5350	386.1 ± 83.2	3.32	m
N_2H^+ (1−0)	93 173.7	2.36 ± 0.42	5353.0 ± 8.9	386.3 ± 20.6	5.42	*m*
$C^{34}S$ (2−1)	96 412.9	1.19 ± 0.14	5393.6 ± 35.7	450	2.46	*t*
CH_3OH (2_k−1_k)	96 741.4	0.88 ± 0.09	5350	390	2.09	*m*, *t*
CS (2−1)	97 981.0	4.15 ± 0.07	5342.6 ± 4.7	408.1 ± 10.7	9.14	
HC_3N (11−10)	100 076.4	4.17 ± 0.11	5331.4 ± 7.4	386.7 ± 17.4	10.00	
HC_3N, $v7 = 1$ (11_1−10_{-1})	100 322.4	0.99 ± 1.01	5331	390	2.38	
HC_3N, $v7 = 1$ (11_{-1}−10_1)	100 466.2	0.99 ± 1.01	5331	390	2.39	
HC_3N (12−11)	109 173.6	4.91 ± 0.14	5331.4 ± 7.4	386.7 ± 17.4	11.78	
HC_3N, $v6 = 1$ (12−11)	109 422.0	1.36 ± 1.01	5331	390	3.28	
HC_3N, $v7 = 1$ (12_1−11_{-1})	109 598.8	1.37 ± 1.01	5331	390	3.29	
$C^{18}O$ (1−0)	109 782.2	4.48 ± 0.25	5330	450	9.02	*b*
HNCO ($5_{0,5}$−$4_{0,4}$)	109 905.8	1.05 ± 0.39	5344.2 ± 84.4	367.0 ± 197.3	2.64	*m*, *b*
^{13}CO (1−0)	110 201.4	4.83 ± 0.25	5330	450	9.71	*b*
CH_3CN (6_k−5_k)	110 383.5	1.77 ± 0.26	5350	386.1 ± 83.2	4.18	*m*, *b*
CN ($1_{0,1}$−$0_{0,1}$)	113 191.3	2.98 ± 0.08	5365.4 ± 10.4	532.4 ± 19.8	4.92	*m*
CN ($1_{0,2}$−$0_{0,1}$)	113 491.0	5.94 ± 0.16	5365.4 ± 10.4	532.4 ± 19.8	9.67	*m*
^{12}CO (1−0)	115 271.2	94.90 ± 0.18	5336.2 ± 9.3	429.0 ± 0.9	207.80	

Notes. See caption of Table A.1 for details.

Table A.8. Results for Mrk 231.

Line	Frequency MHz	I K km s^{-1}	$V_{\rm LSR}$ km s^{-1}	ΔV km s^{-1}	$T_{\rm MB}^{\rm peak}$ mK	Comments
$H^{13}CN$ (1−0)	86 340.2	0.46 ± 0.10	12 053.5 ± 29.4	210	2.02	*hf*, *t*
C_2H (1−0)	87 316.9	0.57 ± 0.11	12 007.0 ± 35.1	210	1.46	*hf*, *t*
HCN (1−0)	88 631.8	2.06 ± 0.12	11 973.2 ± 8.0	207.8 ± 18.3	8.86	*hf*
HCO^+ (1−0)	89 188.6	1.34 ± 0.09	11 951.0 ± 10.9	234.0 ± 25.1	5.23	
HNC(1−0)	90 663.6	0.68 ± 0.14	11 975.6 ± 28.3	204.7 ± 65.9	3.06	
HC_3N (10−9)	90 979.0	0.25 ± 0.06	12 067.4 ± 33.4	210	1.10	t
CS (2−1)	97 981.0	0.44 ± 0.09	12 048.0 ± 27.4	210	1.96	t
HC_3N (11−10)	100 076.4	0.32 ± 0.08	12 067.4 ± 33.4	210	1.40	t
HC_3N (12−11)	109 173.6	0.38 ± 0.09	12 067.4 ± 33.4	210	1.68	*t*
$C^{18}O$ (1−0)	109 782.2	0.35 ± 0.06	12 056.6 ± 23.7	210	1.57	
^{13}CO (1−0)	110 201.4	0.41 ± 0.06	12 086.1 ± 21.2	210	1.81	
CN ($1_{0,1}$−$0_{0,1}$)	113 191.3	0.31 ± 0.21	12 066.7 ± 8.5	218.7 ± 19.4	1.32	*m*, *t*
CN ($1_{0,2}$−$0_{0,1}$)	113 491.0	0.82 ± 0.22	12 066.7 ± 8.5	218.7 ± 19.4	3.46	*m*
^{12}CO (1−0)	115 271.2	12.98 ± 1.29	12 038.6 ± 7.8	210	44.25	

Notes. See caption of Table A.1 for details.